A&A, 691, A162 (2024)
https://doi.org/10.1051/0004-6361/202450086

Astronomy & Astrophysics

The Galaxy Activity, Torus, and Outflow Survey (GATOS)

V. Unveiling PAH survival and resilience in the circumnuclear regions of AGNs with JWST

I. García-Bernete[1,2,⋆], D. Rigopoulou[2,3], F. R. Donnan[2], A. Alonso-Herrero[1], M. Pereira-Santaella[4], T. Shimizu[5], R. Davies[5], P. F. Roche[2], S. García-Burillo[6], A. Labiano[1,7], L. Hermosa Muñoz[1], L. Zhang[8], A. Audibert[9,10], E. Bellocchi[11,12], A. Bunker[2], F. Combes[13], D. Delaney[14], D. Esparza-Arredondo[9,10], P. Gandhi[15], O. González-Martín[16], S. F. Hönig[15], M. Imanishi[17,18], E. K. S. Hicks[14,8], L. Fuller[8], M. Leist[8], N. A. Levenson[19], E. Lopez-Rodriguez[20], C. Packham[8,17], C. Ramos Almeida[9,10], C. Ricci[21], M. Stalevski[22,23], M. Villar Martín[24], and M. J. Ward[25]

(Affiliations can be found after the references)

Received 22 March 2024 / Accepted 6 September 2024

ABSTRACT

This study analyses JWST MIRI/MRS observations of the infrared (IR) polycyclic aromatic hydrocarbon (PAH) bands in the nuclear (~0.4″ at 11 μm; ~75 pc) and circumnuclear regions (inner ~kpc) of local active galactic nuclei (AGNs) from the Galactic Activity, Torus, and Outflow Survey (GATOS). We examine the PAH properties in the circumnuclear regions of AGNs and the projected direction of AGN-outflows and compare them to those in star-forming regions and the innermost regions of AGNs. This study employs 4.9–28.1 μm sub-arcsecond angular resolution data to investigate the properties of PAHs in three nearby sources (D_L ~ 30–40 Mpc). Our findings are aligned with previous JWST studies, demonstrating that the central regions of AGNs display a larger fraction of neutral PAH molecules (i.e. elevated 11.3/6.2 and 11.3/7.7 μm PAH ratios) in comparison to star-forming galaxies. We find that AGNs might affect not only the PAH population in the innermost region, but also in the extended regions up to ~kpc scales. By comparing our observations to PAH diagnostic diagrams, we find that, in general, regions located in the projected direction of the AGN-outflow occupy similar positions on the PAH diagnostic diagrams as those of the innermost regions of AGNs. Star-forming regions that are not affected by the AGNs in these galaxies share the same part of the diagram as star-forming galaxies. We also examined the potential of the PAH-H_2 diagram to disentangle AGN-versus-star-forming activity. Our results suggest that in Seyfert-like AGNs, the illumination and feedback from the AGN might affect the PAH population at nuclear and kpc scales, particularly with respect to the ionisation state of the PAH grains. However, PAH molecular sizes are rather similar. The carriers of the ionised PAH bands (6.2 and 7.7 μm) are less resilient than those of neutral PAH bands (11.3 μm), which might be particularly important for strongly AGN-host coupled systems. Therefore, caution must be applied when using PAH bands as star-formation rate indicators in these systems even at kpc scales, with the effects of the AGN being more important for ionised ones.

Key words. techniques: high angular resolution – techniques: spectroscopic – galaxies: active – galaxies: nuclei – galaxies: Seyfert – infrared: galaxies

1. Introduction

The impact of the energy released by an active galactic nuclei (AGNs) in their surrounding environment has been proposed as a key mechanism for regulating star formation (SF) in their host galaxies. Overall, AGN feedback is needed in cosmological simulations to reproduce the observed number of massive galaxies through the quenching of star formation (e.g. Croton et al. 2006; Bongiorno et al. 2016). A significant fraction of AGN positive and/or negative feedback occurs at circumnuclear scales (inner hundreds of pc) in local active galaxies, where large amounts of dust and gas are located, surrounding the AGN (Antonucci 1993). ALMA observations detected the molecular dusty torus in several nearby AGNs and showed that it is part of the galaxy gas flow cycle (e.g. García-Burillo et al. 2016, 2019, 2021, 2024; Alonso-Herrero et al. 2018; Imanishi et al. 2018, 2020, and references therein).

The dust surrounding the central engine absorbs a significant part of AGN radiation and then reprocesses it to emerge in the infrared (IR; e.g. Pier & Krolik 1992). In these dusty environments, optical wavelengths are also heavily affected by dust obscuration, making the IR an ideal spectral range to investigate the inner regions of AGNs (see Ramos Almeida & Ricci 2017 for a review). Luminous quasi-stellar objects (QSOs; $\log L_{bol}$ [erg s^{-1}] $\gtrsim 10^{46}$) are the most powerful AGN, but their key coupling mechanisms remain generally spatially unresolved, except for nearby sources (e.g. Jarvis et al. 2021; Ramos Almeida et al. 2022). Mid-IR sub-arcsecond angular observations (<0.5″) of local AGNs (at distances of ~tens of Mpc) enable us to probe their nuclear and circumnuclear regions (inner ~100 pc scales). There is also evidence that the circumnuclear dusty material observed in local AGNs is not different in terms of their characteristic properties, such as the temperature, to those in distant and luminous QSOs (e.g. Bosman et al. 2024). Therefore, the study of local AGNs can also contribute to our better understanding of distant AGNs.

Polycyclic aromatic hydrocarbons (PAHs) are particles at the smaller end of the interstellar medium (ISM) dust distribution. They are ubiquitous in local sources (see e.g. Li 2020

⋆ Corresponding author; igbernete@gmail.com

for a review), but also in high-z galaxies (e.g. Spilker et al. 2023). These PAH molecules and dust grains play a key role by catalysing and enriching the ISM with organic molecules and in the photoelectric heating of the ISM (Tielens 2005, 2021). They absorb a significant fraction of UV and optical photons from (mainly) young stars (e.g. Peeters et al. 2004), as well as (partially) from old stars when present (e.g. Kaneda et al. 2008; Li & Draine 2002; Zhang & Ho 2023a; Ogle et al. 2024), resulting in their excitation. The excited PAH molecules produce IR features (the brightest bands are 3.3, 6.2, 7.7, 8.6, 11.3, 12.7, and 17.0 μm; e.g. Tielens 2008) through vibrational relaxation (e.g. Draine & Li 2007). Thus, PAH features are considered excellent tracers of the star formation activity in star-forming galaxies (e.g. Rigopoulou et al. 1999; Peeters et al. 2004), but also in AGNs (e.g. Diamond-Stanic & Rieke 2012). The 3.3, 11.3, 12.7, and 17 μm bands are attributed to neutral PAH molecules, whereas the 6.2 and 7.7 μm bands originate mostly from ionised PAH molecules (e.g. Allamandola et al. 1989; Draine & Li 2001; Draine et al. 2021). Using 10-m class ground-based telescopes and N-band (7.5–13 μm) observations, nuclear 11.3 μm PAH emission (a few tens of pc) has been detected in local AGNs (e.g. Hönig et al. 2010; González-Martín et al. 2013; Sales et al. 2013; Alonso-Herrero et al. 2014, 2016; Esquej et al. 2014; Ramos Almeida et al. 2014, 2023; Ruschel-Dutra et al. 2014; García-Bernete et al. 2015, 2019, 2022a; Martínez-Paredes et al. 2015, 2019; Jensen et al. 2017; Esparza-Arredondo et al. 2018). However, these works were limited to the 11.3 μm PAH feature, due to the limited wavelength coverage and sensitivity of ground-based mid-IR observation, which made it impossible to study the effect of AGNs on the properties of PAH molecules.

Previous observations also show lower equivalent widths of all the PAH bands in AGNs compared to those observed in star-forming galaxies (e.g. Alonso-Herrero et al. 2014; García-Bernete et al. 2017, 2022b). Therefore, it has been proposed that PAH features appear to be diluted by the strong AGN continuum (e.g. Alonso-Herrero et al. 2014; Ramos Almeida et al. 2014) and PAH molecules are destroyed by the hard radiation field of the AGN (e.g. Roche et al. 1991; Voit 1992; Siebenmorgen et al. 2004; García-Bernete et al. 2015; Ramos Almeida et al. 2023), or the lack of star-formation activity toward the center of an AGN (e.g. Esparza-Arredondo et al. 2018). Using ground-based N-band observations of the type-2 QSO Mrk 477, Ramos Almeida et al. (2023) reported the non-detection of PAH features in the central ~400 pc of the galaxy. Recently, it was proposed that ionised PAH molecules are preferentially destroyed in AGNs of moderate luminosity ($\log L_{bol}\,[erg\,s^{-1}] < 10^{45.5}$), while neutral PAHs are more resilient (e.g. García-Bernete et al. 2022c,d, and references therein). This is likely related to the fact that the charge distribution within the ionised PAH molecules may affect the strength of its carbon skeleton structure[1]. Ionised PAH molecules have less stable carbon skeletons as a consequence of the increased internal Coulomb forces due the gain or lose of electrons in the molecular system (e.g. Leach 1986; Voit 1992).

To establish the ability of PAHs to trace star-formation activity in these harsh environments, it is essential to understand their molecular properties. However, there is limited knowledge on the effect of hardness of the radiation field, outflows, and shocks on these molecules (e.g. Smith et al. 2007; Diamond-Stanic & Rieke 2010; García-Bernete et al. 2022c,d; Zhang et al. 2022). The relative variations between PAH features indicate different physical conditions (see e.g. Li 2020 for a review). Recent works have already shown the potential of *James Webb* Space Telescope (JWST; Gardner et al. 2023) and Mid-Infrared Instrument (MIRI; Rieke et al. 2015; Wright et al. 2015) Medium Resolution Spectrograph (MRS) to study the properties and composition of PAHs and dusty material in the innermost regions of AGNs (e.g. García-Bernete et al. 2022d, 2024a,b; Lai et al. 2022, 2023; Donnan et al. 2023, 2024a; Zhang & Ho 2023b). Using PAH band ratios, these works also showed that AGNs have a significant impact on the PAH properties in the inner ~100 pc.

Previous spatially resolved maps of the *Spitzer* PAH properties examining the superwind in M 82 demonstrated that the PAH population might favour larger molecules, probably resulting from preferential destruction of smaller PAHs by X-rays and/or shocks (e.g. Beirão et al. 2015; Li 2020). Also, JWST/MRS observations of NGC 7469 show tentative evidence that the PAH population in its outflow regions might be affected by the AGN, having a larger faction of neutral PAH molecules (García-Bernete et al. 2022d). However, the orientation of its nuclear outflow and the weak geometrical coupling between the AGN outflow and the host are not favourable for a definitive study.

In this paper, we report the first detailed characterisation of the PAH properties in the outflow regions of three local AGNs (NGC 5506, NGC 5728 and NGC 7172) with $D_L < 40$ Mpc. In particular, we examine the PAH survival conditions in the circumnuclear regions of AGNs with sources showing different degrees of coupling between its outflow and host galaxy disk. We also compare the observed PAH ratios with model grids (Rigopoulou et al. 2021, 2024). Our results indicate that PAH depletion of the less resilient hydrocarbon populations (ionised ones) may occur in Seyfert-like AGNs even at kiloparsec scales.

The paper is organised as follows. Sections 2 and 3 describe the targets selection, observations, and data reduction. Section 4 gives an overview of the distribution of the molecular and ionised gas and the hardness of the radiation field present in the circumnuclear region. In Sect. 5, we study the impact of in AGN outflows on PAH molecules and explore the potential of the PAH bands as a tool for tracing AGN feedback. Finally, in Sect. 6 we summarise the main conclusions of this work.

2. Targets and observations

The galaxies studied are part of the Galactic Activity, Torus, and Outflow Survey (GATOS; García-Burillo et al. 2021; Alonso-Herrero et al. 2021; García-Bernete et al. 2024a), whose main goal is to understand the properties of the dusty molecular tori and their connection to their host galaxies in local AGNs. The parent sample was selected from the 70th Month *Swift*/BAT AGN catalog, which is flux-limited in the ultra-hard 14–195 keV X-rays band (Baumgartner et al. 2013). We refer to García-Burillo et al. (2021) for details on the GATOS sample selection from the parent sample. The present study employs MIRI/MRS and ALMA observations of a sub-sample of obscured type 1.9/2 AGNs from the GATOS sample. These data are part of the JWST Cycle 1 GO proposal ID 1670 (PI: T. Shimizu and R. Davies). García-Bernete et al. (2024a) presented a first analysis of these observations, primarily focusing on dirty water ices and silicate features. The molecular gas and ionised phases of the outflow of NGC 5728 and NGC 7172 are studied in detail in Davies et al. (2024) and Hermosa Muñoz et al. (2024a). The sub-sample selected for this pilot study cover two orders of magnitude in the observed ionised outflow rate on

[1] Hereafter we will use the term carbon skeleton structure as the backbone of the PAH molecule.

Table 1. Main properties of the AGNs used in this work.

Name	AGN type	D_L (Mpc)	$\log \dot{M}_{out}$ ($M_\odot\,yr^{-1}$)	$\log N_H^{X-ray}$ (cm^{-2})	$\log L_{Bol}^{X-ray}$ ($erg\,s^{-1}$)	i_{disk} (deg)	i_{cone} (deg)	AGN-host coupling
NGC 5506	1.9	27	0.210	22.4	44.31	76	10	Relatively weak
NGC 5728	1.9	39	0.090	24.2	44.23	40	49	Strong
NGC 7172	2	37	0.005	22.9	44.23	88	...	Relatively weak

Notes. The spectral types were taken from Véron-Cetty & Véron (2006). The luminosity distance and spatial scale were calculated using a cosmology with $H_0 = 70\,km\,s^{-1}\,Mpc^{-1}$, $\Omega_m = 0.3$, and $\Omega_\Lambda = 0.7$. The ionised mass outflow rates are from Davies et al. (2020). The intrinsic $L_{14-195\,keV}$ and N_H^{X-ray} were taken from Ricci et al. (2017). Bolometric luminosities are obtained from the 14–195 keV X-ray intrinsic luminosities by multiplying by a factor of 7.42 as in García-Bernete et al. (2019). The inclinations of the disk and ionisation cones are from Fischer et al. (2013), Shimizu et al. (2019) and Alonso-Herrero et al. (2023).

~150 pc scales (~0.005–0.21 $M_\odot\,yr^{-1}$). The AGN bolometric luminosity and distances are rather similar (see Table 1). The targets have been selected to have different degrees of outflow-host galaxy coupling from very strong to weak (see e.g. Fig. 4 in Ramos Almeida et al. 2022). For instance, NGC 5728 has strong coupling ($i_{disk} \sim 40°$ and $i_{bicone} \sim 49°$; Shimizu et al. 2019) while NGC 5606 ($i_{disk} \sim 76°$ and $i_{bicone} \sim 10°$; Fischer et al. 2013) and NGC 7172 have a relatively weaker coupling. Although there is no NLR modelling for NGC 7172, the fitted value of the inclination for the molecular gas disk is $i_{disk} \sim 88°$ (Alonso-Herrero et al. 2023), although the galaxy on a larger scale appears to be at a lower inclination, and the ionised outflow is perpendicular to the disk (e.g. Hermosa Muñoz et al. 2024a). Even if the geometrical coupling is relatively weak compared to NGC 5728, signatures of AGN feedback has been found in NGC 5506 and NGC 7172 (see e.g. Alonso-Herrero et al. 2023; Esposito et al. 2024; Hermosa Muñoz et al. 2024a for further details). For our targets, we assume that the NLR (i.e. ionisation cones) are co-spatial with the main AGN ionised outflow, which is a reasonable assumption given that outflow signatures (i.e. high velocity and velocity dispersion) have been reported in the NLR region of these sources in individual studies (Fischer et al. 2013; Durré & Mould 2018; Shimizu et al. 2019; Alonso-Herrero et al. 2023; Esposito et al. 2024; Davies et al. 2024; Hermosa Muñoz et al. 2024a). The main properties of the galaxies studied here are summarised in Table 1. We refer to Appendix C for further information on the individual objects.

3. Data reduction

3.1. JWST/MIRI-MRS integral field spectroscopy

We used mid-IR (4.9–28.1 μm) MIRI MRS integral-field spectroscopy data. The MRS has a spectral resolution of R ~ 3700–1300 (Labiano et al. 2021) and comprises four wavelength channels: ch1 (4.9–7.65 μm), ch2 (7.51–11.71 μm), ch3 (11.55–18.02 μm), and ch4 (17.71–28.1 μm). These channels are further sub-divided into three sub-bands (short, medium, and long). The field of view is larger for longer wavelengths: ch1 (3.″2 × 3.″7), ch2 (4.″0 × 4.″7), ch3 (5.″2 × 6.″1), and ch4 (6.″6 × 7.″6). The spaxel size is ranging from 0.″13 to 0.″35. We refer to Rieke et al. (2015) and Wright et al. (2015) for further details (see also Argyriou et al. 2023). We primarily followed the standard MRS pipeline procedure (e.g. Labiano et al. 2016, and references therein) to reduce the data using the pipeline release 1.11.4 and the calibration context 1130. Some hot and cold pixels are not identified by the current pipeline version, so we added an extra step before creating the data cubes to mask them. The data reduction is described in detail in García-Bernete et al. (2022d, 2024a) and Pereira-Santaella et al. (2022). The nuclear spectra from the different sub-channels were extracted assuming they are point sources (~0.4″ at 11 μm; see García-Bernete et al. 2024a for further details).

3.2. ALMA data

Observations of the CO(3-2) emission line at 345.796 GHz emission line for the GATOS sample were obtained using ALMA band 7. We refer the reader to García-Burillo et al. (2021) for further details on the ALMA data. The data were obtained as part of programmes #2017.1.00082.S (PI: S. García-Burillo), #2018.1.00113.S (PI: S. García-Burillo) and #2019.1.00618.S (PI: A. Alonso-Herrero). For this work, we used the fully reduced CO(3-2) maps of NGC 5506 and NGC 7172 from García-Burillo et al. (2021) and Alonso-Herrero et al. (2023). The ALMA CO(3-2) data for NGC 5728 were obtained in the compact configuration of the array (C43-4). In total, two tracks were observed using observations on February 27 and 29, 2020. We used a single pointing with a field of view (FoV) of 17″. The data were processed using the standard pipeline data reduction routine and CASA (version 5.6.1-8; McMullin et al. 2007). The continuum in each of the four spectral windows was identified and subtracted by the pipeline before imaging the CO(3-2) line.

4. Mid-infrared circumnuclear emission

4.1. Distribution of the circumnuclear molecular and ionised gas

To study the distribution of the circumnuclear molecular and ionised gas, we produced emission features maps using a local continuum and 3σ signal-to-noise cut[2]. For the emission lines, we used the ALUCINE tool (Peralta de Arriba et al. 2023) with a single Gaussian fit spaxel-by-spaxel covering the entire cube. In the case of the broad PAH features, we first fitted a local continuum that we then subtracted from the observed spectra and integrated the residual data in a spectral range centred in the peak of the bands. We used the 6.0–6.5 μm and 11.05–11.6 μm for the 6.2 and 11.3 μm PAH features, respectively (see García-Bernete et al. 2022d for further details). We follow the same methodology as presented in Hernán-Caballero & Hatziminaoglou (2011). We also degraded the maps to the coarser angular resolution when comparing directly (e.g. ratio maps). To do so, we first convolve the higher angular resolution maps with a Gaussian to match the size of the PSF star at the wavelength of the lower angular resolution map. In particular, we employed observations of calibra-

[2] We use the continuum to estimate the AGN position for each sub-channel.

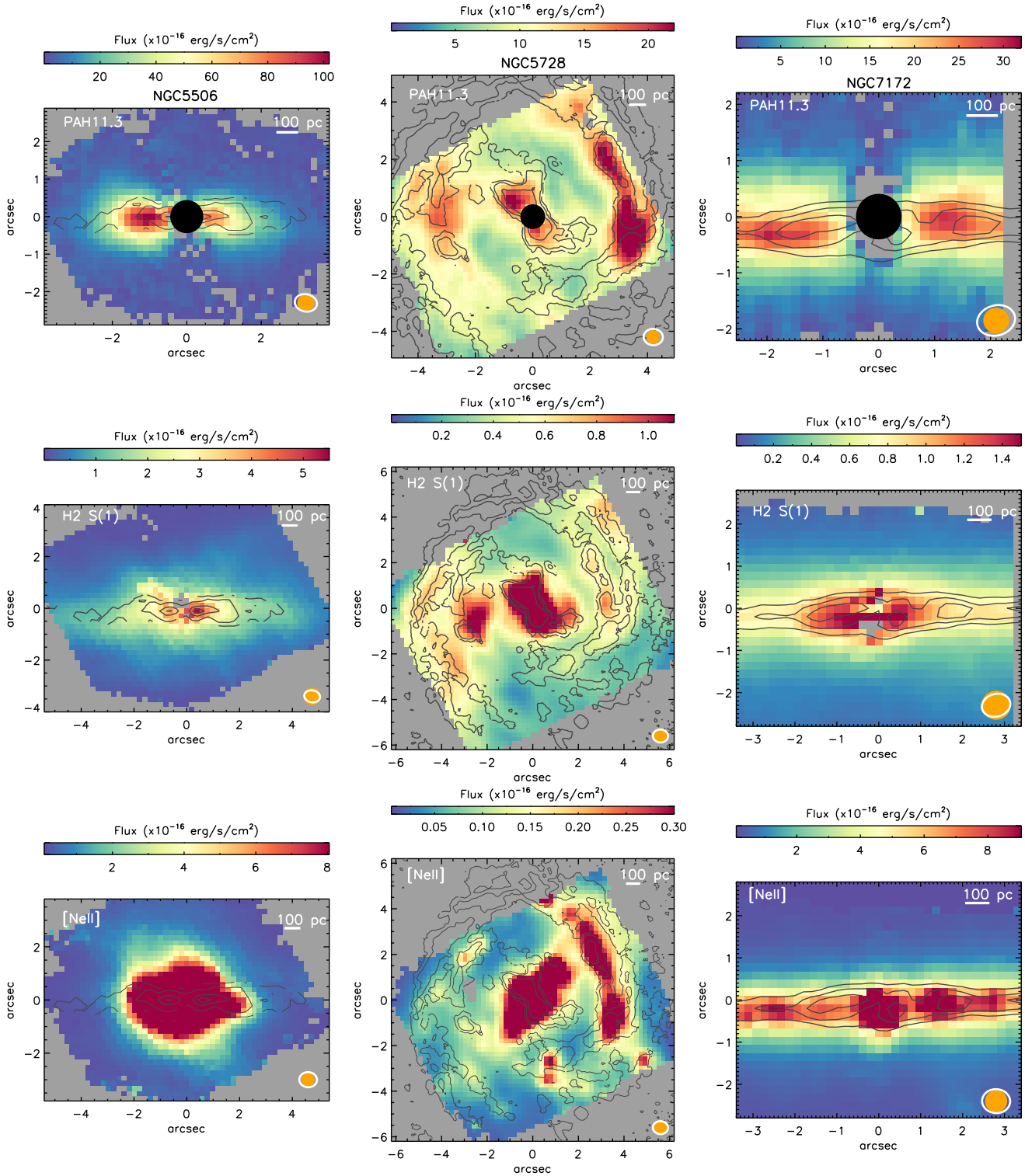

Fig. 1. JWST/MRS emission line maps. From left to right: NGC 5506, NCG 5728 and NGC 7172. Top panels: 11.3 µm PAH feature intensity map. Central panels: H_2 S(1) at 17.03 µm intensity map. Bottom panels: [Ne II] 12.81 µm intensity map. The black contours are the CO(3-2) emission from ALMA on a logarithmic scale. The first and last contours lie at 3σ and the peak flux, respectively. North is up and east is to the left, and offsets are measured relative to the AGN. Orange solid circle and white ellipse correspond to the JWST and ALMA beams, respectively.

tion point sources (HD-163466 and IRAS 05248−7007, Program IDs 1050 and 1049, PIs: B. Vandenbussche and M. Migo Mueller) to measure the FWHM of the PSF for each spectral channel. Then, we resampled the pixel size of the shorter wavelength map to match that of longer wavelength one for each pair.

In Fig. 1, we show the 11.3 µm PAH feature (top panels) and H_2 0-0 S(1) 17.03 µm (bottom panels) intensity map for NGC 5728, NGC 7172, and NGC 5506 (from left to right panels). In general, the 11.3 µm PAH maps reveal a good correspondence with the morphology of the cold molecular gas (black contours in Fig. 1) traced by ALMA CO (3-2). Performing a spaxel-

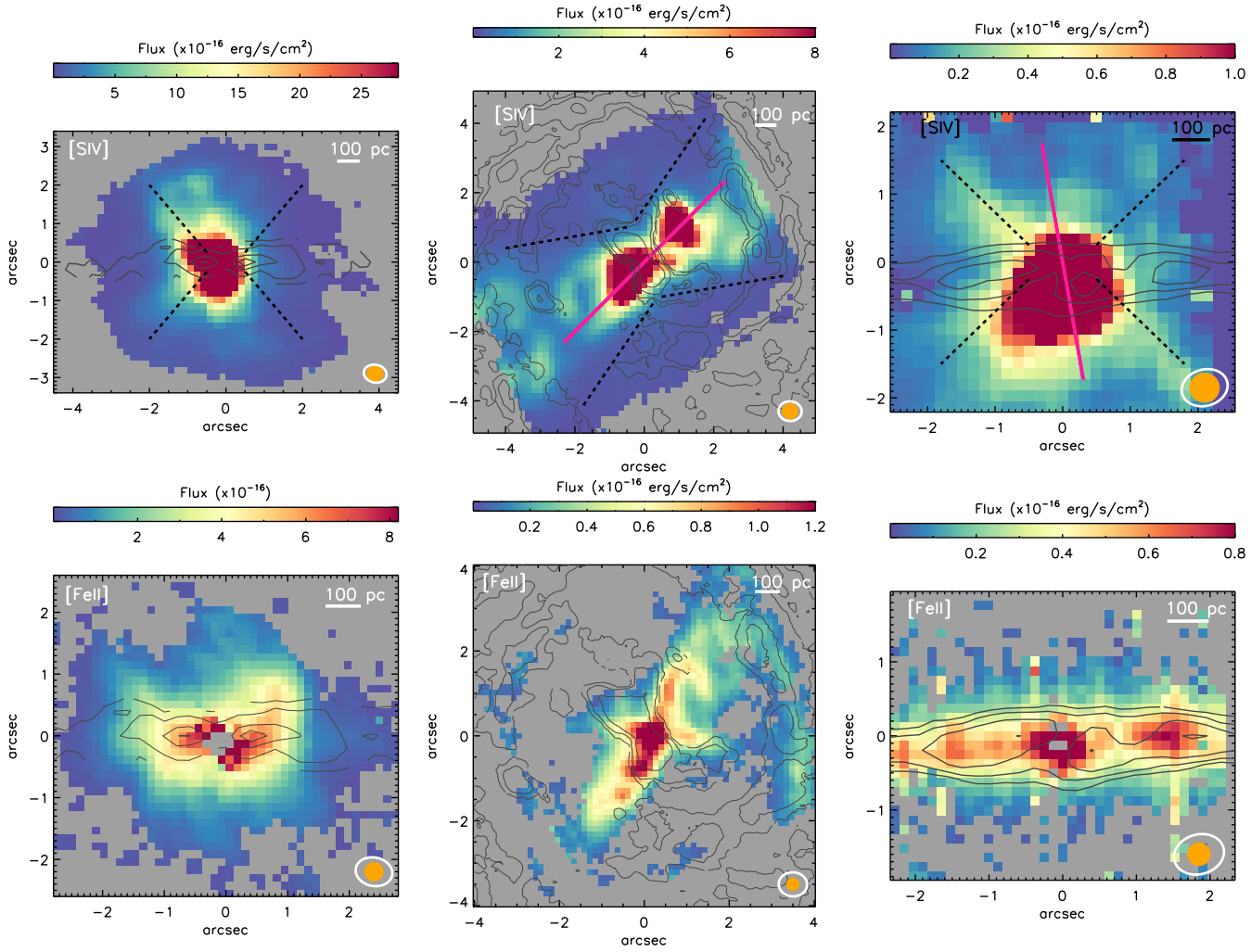

Fig. 2. JWST/MRS emission line maps. From left to right: NGC 5506, NCG 5728 and NGC 7172. Top panels: [S IV] 10.51 μm intensity map. Magenta solid lines represent the radio jet axis (from Thean et al. 2000; Kinney et al. 2000; Shimizu et al. 2019). Bottom panels: [Fe II] 5.34 μm intensity map. The black contours are the CO(3-2) emission from ALMA (same as in Fig. 1). North is up and east is to the left, and offsets are measured relative to the AGN. Orange solid circle and white ellipse correspond to the JWST and ALMA beams, respectively.

by-spaxel analysis, NGC 5506 and NGC 7172 show a tight correlation between the 11.3 μm PAH band and CO (3-2) emission (see Table 2). For NGC 5728, there is also a remarkably good agreement between the CO(3-2) molecular gas and the 11.3μm PAH emission in the inner circumnuclear structure. However, within various circumnuclear regions of NGC 5728, cold and warm molecular gas emission is present in zones where the emission of PAHs and low ionisation potential (IP) lines such as [Ne II] is weak (see central bottom panel of Fig. 1; see also Davies et al. 2024). The PAH emission might also be excited by the ISM radiation field from old stars (e.g. Kaneda et al. 2008; Ogle et al. 2024), however, the observed weak [Ne II] emission (see bottom panels of Fig. 1) suggests that in these regions there are cold molecular gas clumps, which are not (yet) actively forming stars.

Although there is a good relationship between CO(3-2) cold molecular gas and the 11.3 μm PAH emission in the central region of NGC 5728, they are not well correlated when considering the entire FoV (see Table 2). Similarly, the H_2 0-0 S(1) warm molecular gas and the 11.3 μm PAH emission show a poor correlation in NGC 5728, while these are tight for NGC 5506 and NGC 7172 (see Table 2).

Table 2. Pearson's correlation coefficients.

Galaxy	PAH 11.3 μm vs. H_2 S(1)	PAH 11.3 μm vs. CO (3-2)	H_2 S(1) vs. CO (3-2)
NGC 5506	**0.79** (249)	0.61 (311)	**0.76** (1049)
NGC 5728	0.36 (1725)	0.24 (1424)	**0.79** (1393)
NGC 7172	**0.73** (630)	**0.88** (818)	**0.87** (1014)

Notes. Values in parentheses correspond to the number of spaxels considered in the correlation. In bold, we indicate relatively strong correlations (i.e. $\rho > 0.7$).

The cold molecular gas from ALMA and the warm phase traced by the H_2 0-0 S(1) show an excellent correlation in the three galaxies studied here (see Table 2; see also Davies et al. 2024 for a comparison with CO(2-1) for NGC 5728). However, some H_2 0-0 S(1) excess with respect to the cold molecular gas emission can be found in the same direction of the ionisation cones, which is probably related to shocks in the outflow direction (e.g. Kristensen et al. 2023, and references therein).

The ionisation cone region as probed by the high-excitation line emission ([S IV] 10.51 μm; top panels of Fig. 2) extends out

to ∼1 kpc in NGC 5728, and at least hundreds of pc in NGC 5506 and NGC 7172 (also Esposito et al. 2024; Hermosa Muñoz et al. 2024a; Zhang et al. 2024a; Delaney, in prep.). NGC 5728 shows extended [S IV] 10.51 µm emission, which is in agreement with previous works (e.g. Shimizu et al. 2019; Davies et al. 2024, and references therein). NGC 7172 and NGC 5506 show a more compact [S IV] emission as probed by the FoV of the observations, but still elongated in the direction of the ionised outflow of these sources (e.g. Fischer et al. 2013; Alonso-Herrero et al. 2023; Esposito et al. 2024; Hermosa Muñoz et al. 2024a). Furthermore, two (NGC 5728 and NGC 7172) of the three galaxies have radio emission with the same orientation as the ionised cone (see Fig. 2 and Appendix C for further details on the individual objects). The position angle of the extended radio emission in NGC 5506 is ∼70° (Schmitt et al. 2001), which has a similar morphology to that of the [S IV] map presented in Fig. 2. Depending on the geometrical coupling, these relatively low luminosity radio jets can inject additional mechanical energy to the ISM of the galaxy disks (e.g. Combes et al. 2013; García-Burillo et al. 2014; Morganti et al. 2015; Bellocchi et al. 2019; García-Bernete et al. 2021; Venturi et al. 2021; Peralta de Arriba et al. 2023; Audibert et al. 2023; Ogle et al. 2024; Speranza et al. 2024). The [Fe II] 5.34 µm intensity maps (bottom panels of Fig. 2) are a good tracer of shock and star-forming activity (e.g. Spinoglio et al. 2002; Allen et al. 2008). These maps show that shocks are likely operating in the outer edges of the ionisation cones in NGC 5728 and NGC 5506, where [Fe II] emission is detected beyond the central cold molecular gas emission. However, the similar morphology of the circumnuclear cold molecular gas and [Fe II] emission in NGC 7172 suggests that the [Fe II] emission in this source could be mainly related to star-forming activity. However, this might be not the case for the nuclear region, where [Fe II] emission is strong while there is a deficit of CO (3-2).

4.2. Hardness of the radiation field

There is evidence that AGNs might have a significant impact on the PAH molecules located in their nuclear regions (e.g. García-Bernete et al. 2022d, and references therein). Thus, it is important to better understand the effect of the radiation fields on these molecules. The [Ne III] 15.55 µm/[Ne II] 12.81 µm ratio is a reliable indicator of the hardness of the radiation field in the surroundings of massive young stars (e.g. Thornley et al. 2000). This ratio can also be applied in the context of AGNs (e.g. Groves et al. 2006; Pereira-Santaella et al. 2010; García-Bernete et al. 2022c); however, low IP emission lines such as [Ne II] can be significantly contaminated by the X-ray-dominated regions in AGNs (e.g. García-Bernete et al. 2017; Pereira-Santaella et al. 2017). Thus, as a sanity check, we also used other ratios with higher IP lines, such as [Ne V], and found similar results.

Top panels of Fig. 3 shows the spatially resolved [Ne III]/[Ne II] ratio maps of NGC 5728, NGC 7172, and NGC 5506 (from left to right). As expected, these maps show a good correspondence between the location of the ionisation cone and the higher values of the [Ne III]/[Ne II] ratio map. Lower values of this ratio (associated with star-forming activity; magenta contour in top panels of Fig. 3) are found in the galaxy disk of NGC 7172 (see Hermosa Muñoz et al. 2024a for a detailed discussion) and NGC 5506 and in three regions in the star-forming ring of NGC 5728 (see top left panel of Fig. 3). Interestingly, although the majority of the high [Ne III]/[Ne II] value spaxels of NGC 5728 are mainly located along the main outflow axis, it has also high [Ne III]/[Ne II] values in the perpendicular direction to the jet[3]. This perpendicular region also shows high-velocity dispersion values in high IP lines (e.g. [S IV], [Ne III], [Ne V] 14.32 µm, 24.32 µm and warm H_2 lines; see Fig. 4, also Davies et al. 2024). Previous studies have reported a similar high-velocity dispersion structure perpendicular to the direction of the outflow in the presence of a geometrically coupled radio jet (e.g. Ogle et al. 2024), as demonstrated by using ionised gas traced by optical lines (Venturi et al. 2021) and cold molecular gas from ALMA (Audibert et al. 2023). This has been also found in a sample of low-ionisation nuclear emission-line region galaxies (LINERs) with no radio jet (e.g. Hermosa Muñoz et al. 2024b). A number of possible effects could account for this high-velocity dispersion enhancement: (1) jet-induced acceleration of gas out of the disc plane (e.g. Audibert et al. 2023; Venturi et al. 2021); (2) outflowing torus (e.g. Alonso-Herrero et al. 2018); (3) broad AGN outflows, which might potentially resemble a spherical bubble. Beam smearing could also affect the velocity dispersion, however, this velocity dispersion enhancement has also been detected in the ALMA observations of NGC 5728 (see e.g. Fig. 3 of Shimizu et al. 2019). Given the geometrical coupling of the jet and the host galaxy disk in NGC 5728, the first scenario is most likely, although a detailed kinematic analysis is needed to confirm this. We refer to Davies et al. (2024) for further discussion of the outflow of this galaxy.

5. PAH bands as a tool for tracing AGN feedback

There is consensus that the stretching and bending vibrations involving the C-H and C-C bonds produce the observed PAH bands (e.g. Li 2020 for a review). In particular, ionised PAH molecules are responsible for 6–9 µm features, whereas the 3.3, 11.3, and 17 µm features originate in neutral PAH molecules (e.g. Allamandola et al. 1989; Draine & Li 2007; Draine et al. 2021). Therefore, the ratios between the 11.3 µm feature and those related to the charged PAHs (i.e. 6.2 or 7.7 µm features) have been proposed as a good indicator of the PAH ionisation fraction (e.g. Draine & Li 2001, 2007; Draine et al. 2021; Rigopoulou et al. 2021). The IP of PAH molecules is small (∼few eV; e.g. Wenzel et al. 2020). Previous works using *Spitzer*/IRS data found that AGN-dominated galaxies have an average 11.3/6.2 PAH ratio of ∼2, whereas star-forming galaxies have an average ratio of 1 (García-Bernete et al. 2022c). This trend has also been found in the central region of AGNs with high angular resolution JWST observations of nearby sources (e.g. García-Bernete et al. 2022d). This indicates that the central region of AGNs might contain a larger fraction of neutral PAH molecules compared to star-forming regions. However, investigating a larger sample is needed to firmly confirm this trend.

Here, we investigate how the PAH ionisation fraction changes spatially in the JWST/MRS FoV for the three galaxies. In bottom panels of Fig. 3, we present the spatially resolved 11.3/6.2 PAH maps. These plots show that the fraction of neutral PAH molecules is similar in the star-forming ring of NGC 5728 compared to those of the inner circumnuclear region (i.e. the minispiral region, which is extended in the same direction as the dusty torus; see Alonso-Herrero et al. 2018). The map also reveals regions where the neutral PAHs generally dominate along the projected direction of the outflow (Fig. 3). While this effect is evident for NGC 5728 in Fig. 3, it is not as clear for the

[3] We note that Venturi et al. (2021) also reported AGN-dominated LINER-like excitation in the perpendicular direction to the jet in some local AGNs using the optical BPT diagram.

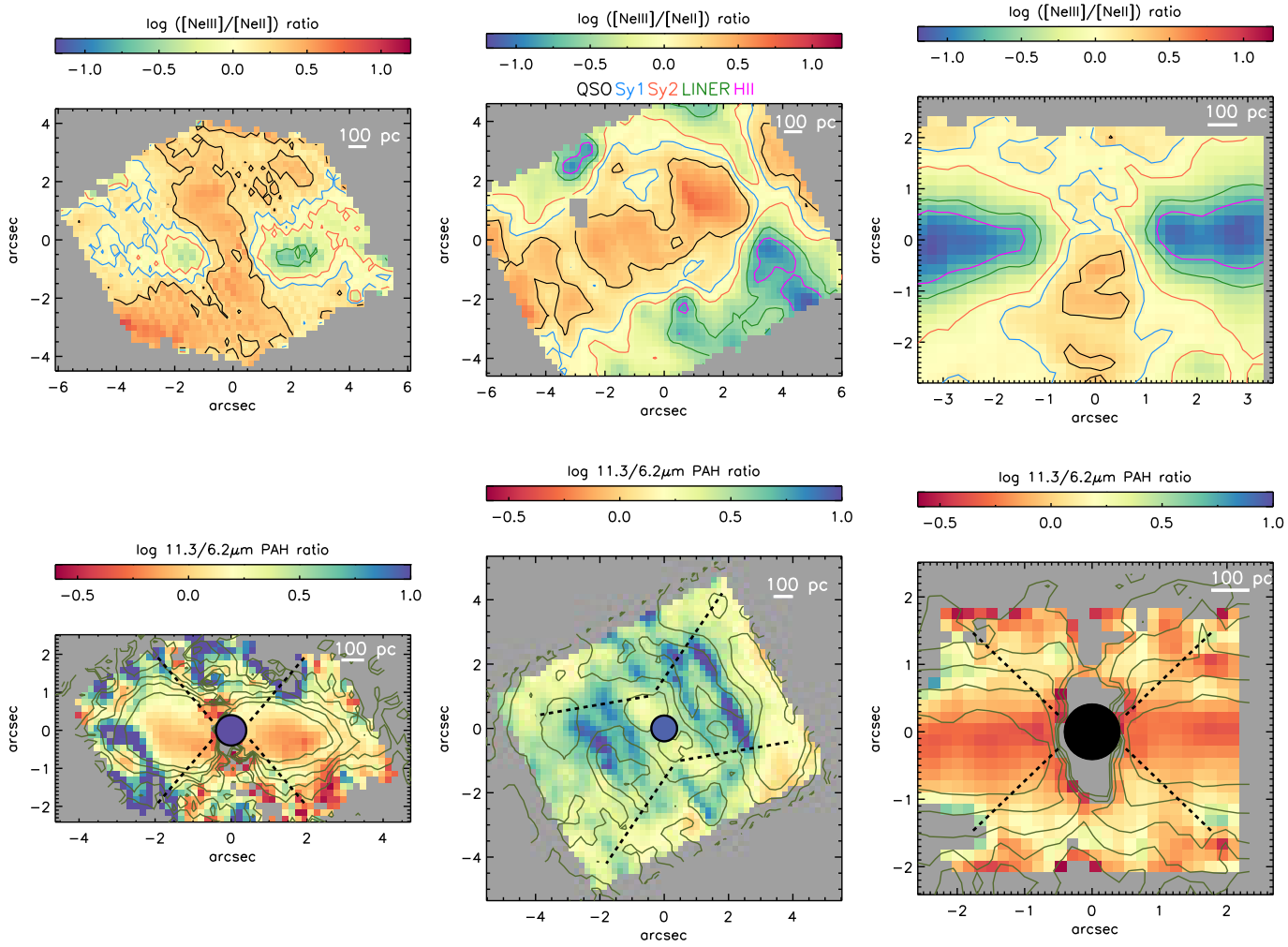

Fig. 3. JWST/MRS spatially resolved maps. From left to right panels: NGC 5506, NCG 5728, and NGC 7172. Top panels: Hardness of the radiation field maps traced by the [Ne III]/[Ne II] ratios. The colour-coded contours correspond to the average [Ne III]/[Ne II] ratios found in QSO (black line), Sy1 (blue line), Sy2 (red line), LINER (green line), and HII (magenta line) regions reported in Pereira-Santaella et al. (2010). Bottom panels: 11.3/6.2 PAH ratio maps. Dark green contours correspond to the 11.3 μm PAH emission. The first contour is at 3σ and the last contour at 1.5×10^{-15} erg s^{-1} cm^{-2}. Colour-coded circles correspond to the nuclear PAH ratios. The central regions correspond to the 11.3/6.2 PAH ratios measured in the nuclear spectra. For NGC 7172, the black circle represent the non-detection of nuclear PAH for this source (see Sect. 5.1 for further details). North is up and east is to the left, and offsets are measured relative to the AGN.

other two sources (i.e. NGC 5506 and NGC 7172). This is likely explained by the faint 6.2 μm PAH emission present in the projected direction of their outflows. Thus, extractions in a larger aperture to increase the signal-to-noise ratio in the faint emission are needed to confirm the larger fraction of neutral PAH molecules in these regions (see Sect. 5.1). There is a larger fraction of ionised PAHs (low 11.3/6.2 PAH ratio values) in the "normal" star-forming regions of NGC 7172 (bottom central panel of Fig. 3) and NGC 5506 (bottom right panel of Fig. 3) when compared to the circumnuclear emission of NGC 5728. The galaxy disks of NGC 5506 and NGC 7172 exhibit a similar 11.3/6.2 PAH ratio to the typical value found in star-forming galaxies ($\lesssim$1; García-Bernete et al. 2022c). This is consistent with the JWST/MRS observations of NGC 7469 (García-Bernete et al. 2022d; Zhang & Ho 2023b) and of a sample of luminous IR galaxies (Rigopoulou et al. 2024), where star-forming regions shows low 11.3/6.2 PAH ratios ($\lesssim$1; see right bottom panel of Fig. 1 in García-Bernete et al. 2022d). Conversely, the extended emission of NGC 5728 exhibits larger values of the 11.3/6.2 PAH ratio, resembling those typically found in AGN-dominated systems (García-Bernete et al. 2022c,d). In addition, the SF-like 11.3/6.2 PAH ratios found in the disk of NGC 5506 and NGC 7172 are in agreement with the relatively low hardness of the radiation field present in these regions (see top panels of Fig. 3).

The larger fraction of neutral PAH molecules present in the extended emission galaxy disk and projected direction of the outflow of NGC 5728 could be related with the depletion of ionised PAH molecules (García-Bernete et al. 2022c,d) due to the hard radiation field present in the FoV probed by the MRS (see also BPT diagram in Shimizu et al. 2019).

Given the nearly face-on geometry of NGC 5728, we cannot rule out the possibility that UV radiation emitted by an evolved stellar population in the bulge might contribute to exciting PAH molecules (e.g. Kaneda et al. 2008; Ogle et al. 2024). Indeed, a large fraction of neutral PAHs are found in regions with relatively soft radiation fields, similar to those observed in the bulges of galaxies (Kaneda et al. 2008). However, stellar population analyses in local AGNs generally show a significant young (6–30 Myr) stellar population present within the central few

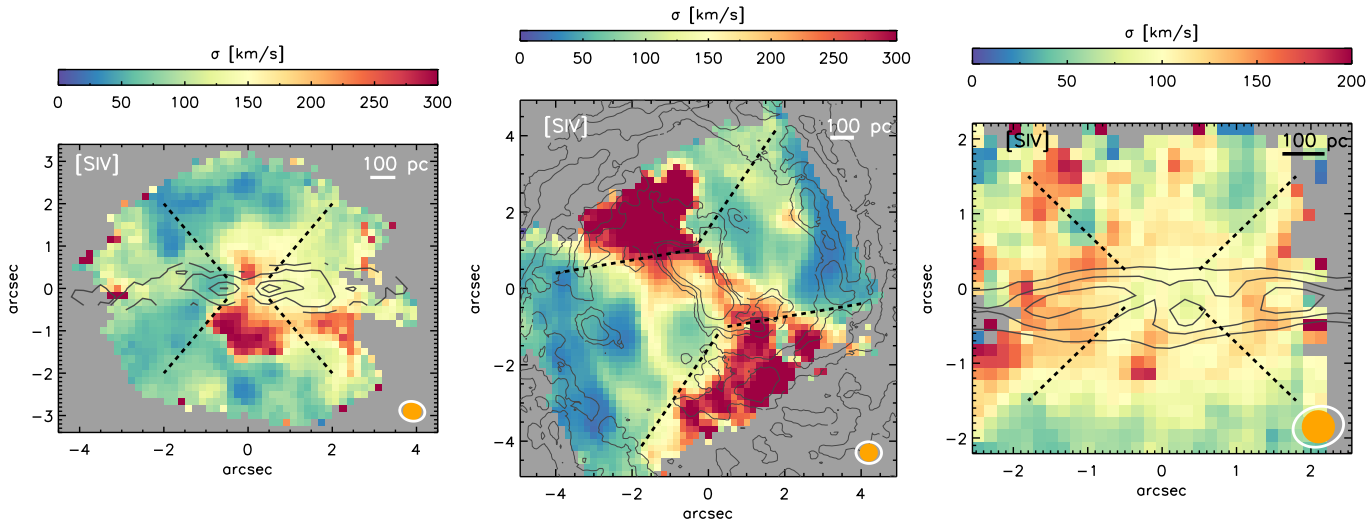

Fig. 4. JWST/MRS [S IV] 10.51 μm velocity dispersion maps. From left to right panels: NGC 5506, NCG 5728 and NGC 7172. The black contours are the CO(3-2) emission from ALMA (same as in Fig. 1). North is up and east is to the left, and offsets are measured relative to the AGN. Orange solid circle and white ellipse correspond to the JWST and ALMA beams, respectively.

hundred parsecs (see e.g. Burtscher et al. 2021, which include two of our targets in their study [NGC 5728 and NGC 7172]). Thus, it is unlikely that an evolved stellar population is significantly contributing to the 11.3 μm PAH emission observed in our targets.

Differences in the PAH ratios might be challenging to identify when using spatially resolved analyses, due to the limited signal-to-noise of the PAH bands. Thus, in Sect. 5.1, we describe how we extracted spectra from various targeted regions that significantly increase the signal-to-noise ratio (S/N) to search for differences in the PAH properties.

5.1. PAH properties in the projected direction of AGN outflows

We compare the relative strengths of the observed PAH bands of AGN- and SF-dominated regions with model grids generated using theoretically computed PAH spectra based on density functional theory (Rigopoulou et al. 2021). In particular, we examined the 6.2/7.7 and 11.3/7.7 μm PAH ratios, which are sensitive to the molecular size and ionisation stage of PAH molecules, respectively. We refer to Rigopoulou et al. (2021) for more details on how these theoretical spectra and grids are constructed.

As the first step, we extracted the JWST/MRS spectra from the nuclear regions of the three sources studied here. We note that the nuclear spectrum of NGC 7172 is strongly dominated by the continuum and shows no PAH emission (see Fig. 1 of García-Bernete et al. 2024a, also Hermosa Muñoz et al. 2024a); thus, its nuclear region is not included in Fig. 5. The high extinction values together with the strong continuum might dilute and attenuate the nuclear PAH emission from the nuclear region, which might be connected to the dust lane present in NGC 7172 (see Appendix C). To investigate the similarities and differences in the PAH properties between nuclear regions, and the projected direction of the outflow, and star-forming zones, we selected a number of circumnuclear regions in the three targets (see Appendix A for further details on the extracted apertures). In Tables A.1 and A.2, we list the measured PAH fluxes in this work.

Left panel of Fig. 5 shows that the nuclear regions (filled squares) of AGNs tend to have large 11.3/7.7 μm PAH ratios (and similarly for the 11.3/6.2 μm PAH ratio) compared to 'normal' SF regions. This suggests that in the nuclear regions of AGNs, the PAH emission originates in neutral PAH molecules with little variation of the molecular sizes[4]. Our findings show the same trend than in previous works, which also include type 1 and 2 AGNs, using JWST/MRS observations (e.g. García-Bernete et al. 2022d). More recently, using JWST observations of local luminous infrared galaxies, Rigopoulou et al. (2024) also found that SF-regions have a larger fraction of ionised PAH molecules compared to that of AGNs.

There is some scatter seen in the PAH band ratios for the nuclear regions of AGNs (see left panel of Fig. 5), indicating that the mean PAH properties might slightly differ from source to source. However, the nuclear regions of AGNs favour larger fractions of neutral PAH molecules compared with star-forming regions (filled stars). Furthermore, SF-dominated regions tend to cluster in a narrower part of the diagram where the location of star-forming galaxies using integrated values from *Spitzer*/IRS lie (García-Bernete et al. 2022c; grey area in Fig. 5). However, PAH molecular sizes traced by 6.2/7.7 μm PAH ratio are rather similar.

Star-forming regions located along the projected direction of the outflow of NGC 5728 (i.e. SF2, SF3, SF4, SF5, SF6, SF7, SF9, and SF10 in Fig. A.1; average value represented by a purple filled triangle in Fig. 5, right) show larger values of the 11.3/7.7 μm PAH ratio than in 'normal' SF regions. We also find high 11.3/7.7 μm PAH ratios in the projected direction of the outflow of NGC 5728 (i.e. Out1, Out2, and Out3 in Fig. A.1) and in the perpendicular region of the jet (high-velocity dispersion region; i.e. D1 and D2 in Fig. A.1). This high-velocity dispersion region has been interpreted as lateral turbulence caused by the jet interacting with the host galaxy (e.g. Venturi et al. 2021). Consequently, the elevated 11.3/7.7 μm (and 11.3/6.2 μm) PAH ratio observed in this region is consistent with this interpretation. The average value of the regions located in the projected direction of the outflow of NGC 5728 is rep-

[4] PAH molecular sizes are estimated by using the 6.2/7.7 μm PAH ratio.

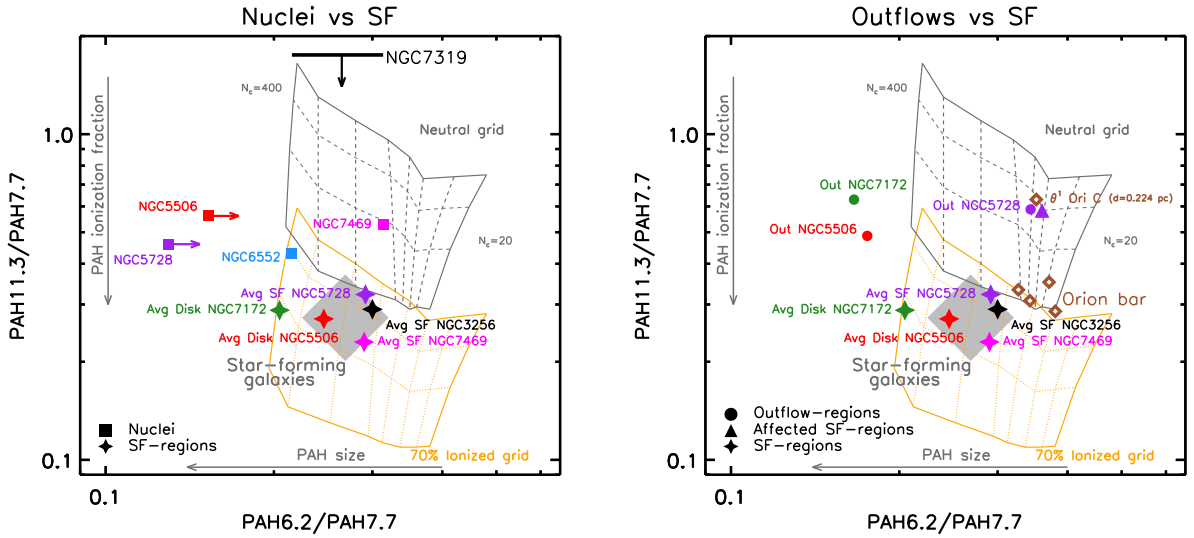

Fig. 5. PAH diagnostic diagram: relative strengths of the 6.2, 7.7, and 11.3 μm PAH features. Left panel: Nuclear regions of AGNs versus star-forming regions. Filled squares correspond to the nuclear regions of NGC 5728 (purple square) and NGC 5506 (red square). We also plot the nuclear regions of NGC 6552 (blue square), NGC 7319 (black upper limit) and NGC 7469 (magenta square) from García-Bernete et al. (2022d). Right panel: Outflow regions of AGNs versus star-forming regions. The red, purple, and green circles correspond to average PAH ratios of the outflow regions of NGC 5506, NGC 5728 and NGC 7172, respectively. The purple triangle represents the average value of star-forming regions of NGC 5728 that are affected by the AGN according to their [Ne III]/[Ne II] ratio. For comparison, we plot PDR-like values from the Orion bar (open brown diamond; see Appendix B for details). The grey shaded region denotes the average location of star-forming galaxies from García-Bernete et al. (2022c) using *Spitzer*/IRS data and black and magenta filled stars correspond to the average value of star-forming regions of NGC 3256 (from Rigopoulou et al. 2024) and NGC 7469 (from García-Bernete et al. 2022d). Filled stars correspond to the average star-forming regions of NGC 5728 (purple star), NGC 7172 (green star) and NGC 5506 (red star). The grey grid corresponds to neutral PAHs ranging from small PAHs (N_C = 20; right side of the grid) to large PAH molecules (N_C = 400; left side of the grid). Dashed grey lines correspond to intermediate numbers of carbons. The orange grid corresponds to 70% of ionised PAH molecules for the same number of carbons as the neutral grid. Dotted orange lines correspond to intermediate numbers of carbons. In Fig. A.4, we show this plot with all the individual regions, and in Tables A.1, A.2, and A.3 we list the measured PAH fluxes.

resented by a purple filled circle in Fig. 5 (see also Fig. A.1). For NGC 5506 and NGC 7172, we extracted regions along the projected direction of the outflow (indicated by red and green circles in Fig. 5; see also Fig. A.1). We find high values of the 11.3/7.7 μm PAH ratio in NGC 5506 (filled red circle in Fig. 5) and NGC 7172 (filled green circle in Fig. 5). These regions are also located where the AGN feedback appears to be stronger in these galaxies (e.g. Fischer et al. 2013; Thomas et al. 2017; Davies et al. 2020; Alonso-Herrero et al. 2023; Esposito et al. 2024; Hermosa Muñoz et al. 2024a; Zhang et al. 2024a).

However, the star-forming regions of NGC 5506 (Disk1 and Disk2 apertures in Fig. A.1), NGC 5728 (i.e. SF1, SF8, SF11 and SF12 in Fig. A.1), and NGC 7172 (Disk1 and Disk2 apertures in Fig. A.1) are consistent with PAH ratios typically found in star-forming galaxies (see Fig. A.1). The outflow is located behind the disk for the southern region of NGC 5506 and the northern region of NGC 7172; thus, they exhibit PAH ratios that broadly resemble those of typical star-forming regions (see Appendix A for further details). The hardness of the radiation field is generally higher in the regions with elevated 11.3/7.7 μm PAH ratio (also for the 11.3/6.2 μm PAH ratio; see Fig. 3). These results are in agreement with the previously observed trend of a larger fraction of neutral PAHs being present in the harsh environment of the active nuclei.

For comparison, in Fig. 5, we also show the PAH ratios of the strongly illuminated photodissociation region (PDR) Orion Bar (open brown diamonds; see Appendix B). We used the extracted regions on the JWST/MIRI MRS observations presented in Peeters et al. (2024, see also Chown et al. 2024; Habart et al. 2024; Pasquini et al. 2024 and Elyajouri et al. 2024). The atomic PDR and dissociation fronts (DF1, DF2, DF3; see Fig. 1 of Peeters et al. 2024) show values which are broadly in agreement with the values found for SF-regions in galaxies[5]. However, the closest H II region (projected distance of ~0.224 pc; Peeters et al. 2024) to the main source of ionising radiation and winds (i.e the O7V-type star θ^1 Ori C) have PAH ratios indicating a large fraction of neutral molecules, similar to those observed in the harsh environments of AGNs.

The geometry of the AGN ionised outflow (and radio jet) with respect to the host galaxy disk (i.e. coupling) is key to understanding AGN feedback (e.g. Ramos Almeida et al. 2022, and references therein). Under the assumption that the majority of the PAH molecules are located in the galaxy disk, geometrical coupling between the outflow and jet and host galaxy might play a key role in explaining the effect of the AGN outflow and radio jet in PAH molecules. Recently, using JWST observations, Donnan et al. (2024b) found that PAHs are kinematically influenced by the AGN-driven outflow in the type 1 AGN, NGC 7469. As mentioned above, the geometry derived from NLR modelling (see Sect. 2 and Appendix C) indicates that the AGN ionised outflow and the radio jet might be strongly impacting the galaxy disk in the case of NGC 5728 (see Fig. C.1 in Appendix C) while the geometrical coupling is relatively weak in NGC 7172 and NGC 5506 (e.g. Fischer et al. 2013; Alonso-Herrero et al. 2023;

[5] Note: the spectra of the Orion bar are extracted in regions with a sub-pc physical resolution regions, as opposed to scales of approximately hundreds of pc in the circumnuclear region for the galaxies studied here. This may explain the slightly different PAH ratios observed in the Orion bar compared to star-forming regions.

Davies et al. 2024; Esposito et al. 2024; Hermosa Muñoz et al. 2024a). We further explore the properties of the PAH population in regions showing hard radiation fields (see Fig. 3), which is co-spatial with the projected direction of the outflow of NGC 5728 (see Davies et al. 2024). In general, selected regions in projected direction of the outflow have elevated 11.3/7.7 (and 11.3/6.2) PAH and [Ne III]/[Ne II] ratios as found in AGN-dominated environments (see also Fig. 3).

Based on the 6.2/7.7 μm PAH ratios, we find that all extracted regions typically fall within the range of PAH sizes (i.e. number of carbon; N_c) covered by the grid ($20 < N_c < 400$). The only exceptions are the nuclear regions of NGC 5506 and NGC 5728, which are located in a region favouring larger PAH molecules (see e.g. Kerkeni et al. 2022). However, the 6.2 and 7.7 μm PAH features in these two nuclei are extremely weak; thus, we consider the 6.2/7.7 μm PAH ratio of NGC 5506 and NGC 5728 as lower limits.

Our findings indicate that regions located in the projected direction of the outflow of the AGN presented here generally have a larger fraction of neutral PAH molecules compared to 'normal' SF regions. This is consistent with the tentative evidence found in the nuclear outflow of NGC 7469 using JWST/MRS data (e.g. García-Bernete et al. 2022d) and in the outflow of the starburst M 82 using *Spitzer*/IRS data (Beirão et al. 2015). The fraction of ionised PAHs in the disk regions of NGC 5506 and NGC 7172 (and regions with low [Ne III]/[Ne II] values in NGC 5728) are in agreement with those measured in star-forming dominated regions. The larger fraction of neutral PAH molecules (11.3/7.7 and 11.3/6.2 μm PAH ratios) in the nuclear regions of AGNs and the projected direction of their outflows suggests that the AGN is affecting the PAH emission in these regions. This could be explained by the potential destruction of the ionised molecules, which are less resilient than neutral ones to harsh radiation fields and shocks (see e.g. García-Bernete et al. 2022d; Li et al. 2022). The ionisation of PAH molecules produces electronic rearrangement and structural changes in the system inducing repulsive forces within the molecule that might end in a 'Coulomb explosion' (Leach 1986; Voit 1992). Previous laboratory works have found that for the small PAH molecule naphthalene ($C_{10}H_8$) Coulomb explosions are important when exposed to >40 eV photons (Leach et al. 1989). As previously noted, we cannot rule out that an evolved stellar population in the bulge of NGC 5728 might also contribute to exciting neutral PAH molecules (e.g. Kaneda et al. 2008; Ogle et al. 2024). However, stellar population analyses do not seem to favour this scenario for NGC 5728 (see e.g. Burtscher et al. 2021). We remark that new observations of local AGNs with JWST will allow for the sample to be enlarged, which will be crucial for obtaining definitive conclusions and for enhancing the statistical significance of the findings presented here.

5.2. PAH-H_2 diagram

As discussed above the 11.3/6.2 PAH ratio traces AGN-dominated regions. Here, we further investigate other ratios involving one of the most AGN-affected PAH bands covered by MIRI/MRS (i.e. the 6.2 μm PAH feature). Together with hard X-rays, high IP lines are powerful tools for unveiling AGN activity. However, recent JWST NIR-to-MIR observations of a deeply embedded AGN showed non-detection of high IP (>100 eV) lines (e.g. García-Bernete et al. 2024b). Furthermore, even ultra-hard X-ray (14–195 keV) Swift/BAT observations are missing a significant fraction of highly absorbed type 2 sources (e.g. Ricci et al. 2015; Mateos et al. 2017; García-Bernete et al. 2019). It is thus crucial to search for alternative tracers of AGNs. Our targets with similar bolometric luminosity, but with different hydrogen column densities (see Table 1), and ranging from strong to weak AGN-host coupling allow us to test the diagnostic power of these tracers.

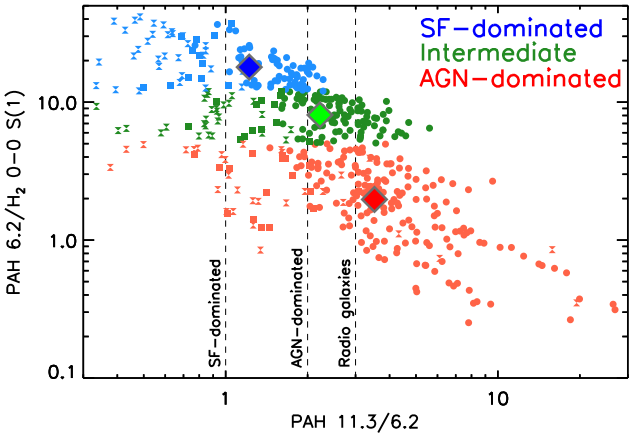

Fig. 6. Relationship between the 11.3/6.2 PAH ratio and 6.2 μm PAH feature relative to H_2 S(1) for all the spaxels of the three targets. Blue, green, and red circles represent values where the 6.2 μm PAH/H_2 S(1) ratio is greater than 12 (SF-dominated), between 12 and 5, and less than 5 (AGN-dominated), respectively. Squares represent the median value of each category. Squares, circles and hourglasses symbols correspond to NGC 5506, NGC 5728, and NGC 7172. The dashed vertical lines represent the average values of star-forming galaxies, AGNs, and relatively powerful radio galaxies from *Spitzer*/IRS observations (Ogle et al. 2010 and García-Bernete et al. 2022c).

We investigated the relation of the 6.2 μm PAH/H_2 0-0 S(1) ratio. H_2 rotational lines originate in warm molecular gas and are excited by UV fluoresence and gas heating by collisional excitation (e.g. Kaufman et al. 2006). Therefore, the H_2 emission depends on the amount of warm molecular gas present, but also on the UV heating and the possible presence of turbulence and shocks (e.g. Kristensen et al. 2023, and references therein). Using *Spitzer*/IRS data, Ogle et al. (2010) found that PAH/H_2 is smaller in jet-powered molecular hydrogen emission galaxies (MOHEGs) with strong jet-ISM interaction compared with 'normal' star-forming galaxies (factor of ~300; see also Nesvadba et al. 2010). The average 11.3/6.2 PAH ratio (~3) reported by Ogle et al. (2010) for relatively powerful radio galaxies[6] is larger than that of AGN[7] (~2; García-Bernete et al. 2022c). Similarly, Labiano et al. (2013, 2014) also found that the 7.7 μm PAH band is weaker than the 11.3 μm PAH feature in relatively powerful radio galaxies[8]. Therefore, 6.2 μm PAH/H_2 is expected to be small in AGNs with strong host-outflow and jet coupling. Recently, JWST/MRS observations have revealed enhanced emission from warm and hot H_2 in NGC 7319 (Pereira-Santaella et al. 2022), which hosts a low-power radio jet and has extremely faint PAH emission (García-Bernete et al. 2022d).

In Fig. 6, we present all the spaxels for the three galaxies at the angular resolution of the H_2 0-0 S(1) maps. Figure 6

[6] Hereafter, we use the terms relatively powerful radio galaxies and MOHEGs interchangeably.

[7] We note that both samples were fitted using PAHFIT (Smith et al. 2007).

[8] Note that the sources studied in Labiano et al. (2013, 2014) are reactivated powerful radio sources, and their radio jets may strongly affect the ISM of the galaxy.

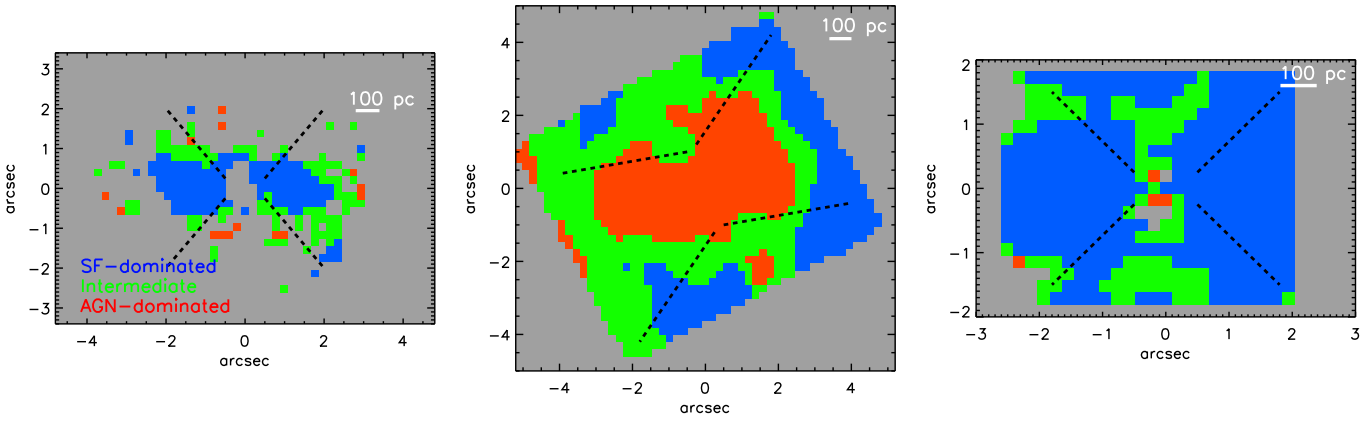

Fig. 7. JWST/MRS 6.2 μm PAH/H_2 S(1) ratio maps. From left to right: NGC 5506, NGC 5728, and NCG 7172. Maps are colour-coded following the criteria in Fig. 6. The SF-, AGN-dominated, and intermediate regions are shown in blue, red, and green, respectively. North is up and east is to the left. Offsets are measured relative to the AGN.

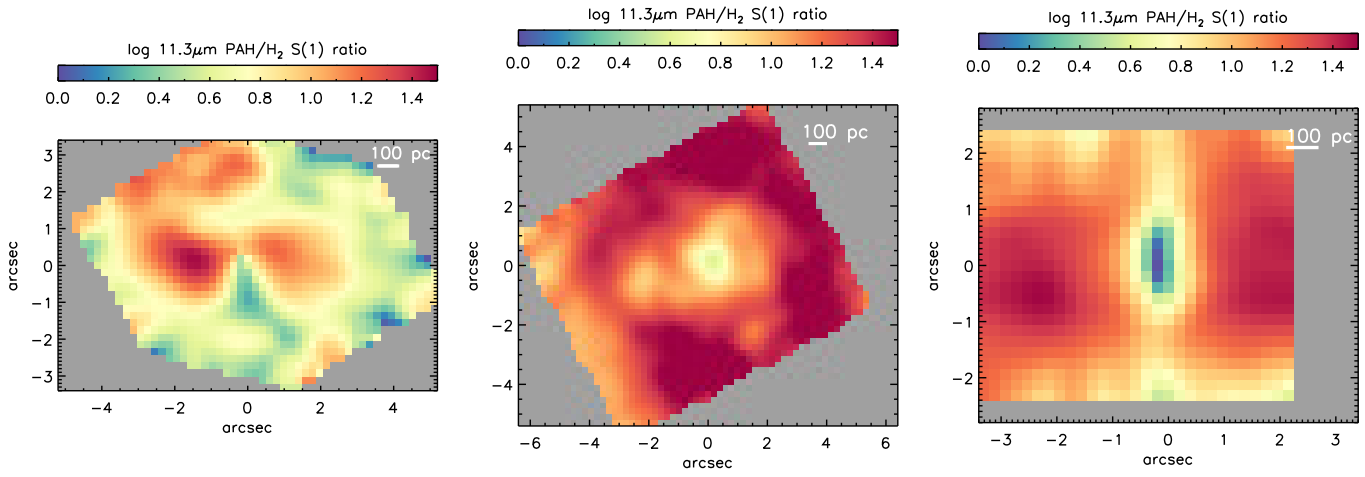

Fig. 8. JWST/MRS 11.3 μm PAH/H_2 S(1) ratio maps. From left to right: NGC 5506, NGC 5728, and NCG 7172. North is up and east is to the left. Offsets are measured relative to the AGN.

shows a relationship between the 11.3/6.2 PAH ratio and the 6.2 μm PAH/H_2 0-0 S(1) ratio. This relation is in part driven by the 6.2 μm PAH feature, which is strongly affected by the AGN, but also by the enhancement of H_2 in AGN-shocked regions. We select regions that are AGN-dominated (red circles) and SF-dominated (blue circles) in Fig. 6. To do so, we use 6.2 μm PAH/H_2 0-0 S(1) < 5 and 6.2 μm PAH/H_2 0-0 S(1) > 12, respectively. To define these values, we compare the 6.2 μm PAH/H_2 0-0 S(1) ratio map with the spatially resolved [Ne III]/[Ne II] maps (see Figs. 3 and 7). As this is a visual criterion, we also included a third classification as intermediate values (5 < 6.2 μm PAH/H_2 0-0 S(1) < 12). The AGN-dominated limit is estimated by using the average value of the 6.2 μm PAH/H_2 0-0 S(1) of those spaxels with [Ne III]/[Ne II] ratios greater than that found for Sy1 in Pereira-Santaella et al. (2010, see top panels of Fig. 3). The 6.2 μm PAH/H_2 0-0 S(1) ratio map of the three targets studied in this work, colour-coded with these criteria, is shown in Fig. 7. Intermediate values of the 6.2 μm PAH/H_2 0-0 S(1) ratio are also found for NGC 7172 where the MIR ionised outflow of this galaxy has been detected (see Hermosa Muñoz et al. 2024a for further discussion on the outflow of this galaxy). NGC 5728 has the largest area of AGN-dominated spaxels (red colour), likely related with the fact that this galaxy shows the strongest outflow-and-jet-host galaxy coupling of the sources studied here. Furthermore, SF-dominated regions are also revealed in the star-forming ring of NGC 5728 and the disk regions of NGC 7172 and NGC 5506 (see Fig. 7). This is in good correspondence with the hardness of the radiation field shown in the top panels of Fig. 3. Ogle et al. (2024) show a similar plot for M 58 to that presented in Fig. 6, but using the 11.3 μm PAH band. Thus, as a sanity check, we also examined the relation of the 11.3 μm PAH/H_2 0-0 S(1) ratio (see Fig. 8) and found a similar results when using the 11.3 μm or 6.2 μm PAH.

Finally, we find that PAH/[Ar II] and PAH/[Ne II] ratios are lower in shock-dominated regions, while this ratio increases in locations where star-forming activity is significant. This together with the results form PAH/H_2 diagnostic suggests that shocks could play a significant role in the PAH-affected regions of AGNs (see also Zhang et al. 2024b for a pilot study examining the potential impact of shocks on PAHs).

6. Summary and conclusions

We present a JWST MIRI/MRS study of the IR PAH bands of the nuclear (~0.4″ at 11 μm; ~75 pc) and circumnuclear regions of local AGNs from the Galactic Activity, Torus, and Outflow Survey (GATOS). In particular, we have investigated the PAH properties in AGN-dominated regions along the projected

direction of the outflow to compare them with those in star-forming regions and AGN nuclei. Our main results are as follows:

1. We find that nuclear regions of intermediate-luminosity AGNs (i.e. Seyfert galaxies) tend to have a larger fraction of neutral molecules (i.e. elevated 11.3/6.2 or 11.3/7.7 PAH ratios), showing the same trend seen in previous works also using JWST/MRS observations (García-Bernete et al. 2022d).
2. We find that even in Seyfert-like AGNs, illumination and feedback from the AGN might affect the PAH population at kpc scales. In particular, the fraction of ionised PAH molecules is low in the outflow zone compared with that of star-forming regions. This result could be explained by the preferential destruction of ionised PAH molecules (i.e. the carriers of the ionised PAH bands; 6.2 and 7.7 μm) in hard environments, such as those found in the circumnuclear regions of AGNs. However, the PAH molecular sizes are rather similar.
3. We find similar trends for integrated PAH/H_2 ratios using high angular resolution spatially resolved maps. In particular, we find that values of the 6.2 μm PAH/H_2 0–0 S(1) > 12 correspond to SF-dominated regions, while those regions with 6.2 μm PAH/H_2 0–0 S(1) < 5 are AGN-dominated. The AGN-dominated limit is estimated by using a standard hardness of the radiation field tracer ([Ne III]/[Ne II] ratios).

All of these results suggest that both AGN feedback and hard AGN radiation fields present in Seyfert-like AGNs, such as those studied in this work, can have a significant impact on the PAH population. This seems to be particularly important for strongly AGN-host-and-jet coupled systems, for which the effects on the PAH molecules located in the disk could be maximal (e.g. NGC 5728). The carriers of the ionised PAH bands (6.2 and 7.7 μm) are less resilient than those of neutral PAH bands (e.g. 11.3 μm). Thus, caution must be applied when using PAH bands as star-formation rate indicators in these systems. Furthermore, PAH bands together with H_2 and low IP emission lines allow for AGN feedback to be disentangled from star-forming activity. This might be especially important for sources where high IP lines are undetected. Future observations of local obscured nuclei using, the unprecedented spatial resolution and sensitivity afforded by the James Webb Space Telescope, will be able to test the potential diagnostic power of the PAH-H_2 classification diagram in buried sources.

Acknowledgements. IGB is supported by the Programa Atracción de Talento Investigador "César Nombela" via grant 2023-T1/TEC-29030 funded by the Community of Madrid. IGB and DR acknowledge support from STFC through grants ST/S000488/1 and ST/W000903/1. We acknowledge support from ESA through the ESA Space Science Faculty Visitor scheme - Funding reference ESA-SCI-SC-LE-212. AAH, LHM, and MVM acknowledge support from grant PID2021-124665NB-I00 funded by MCIN/AEI/10.13039/501100011033 and by ERDF A way of making Europe. MPS acknowledges support from grant RYC2021-033094-I funded by MCIN/AEI/10.13039/501100011033 and the European Union NextGenerationEU/PRTR. SGB acknowledges support from the Spanish grant PID2022-138560NB-I00, funded by MCIN/AEI/10.13039/501100011033/FEDER, EU. AJB acknowledges funding support from the "FirstGalaxies" Grant from the European Research Council (ERC) under the European Union's Horizon 2020 research and innovation pogram (Grant agreement No. 789056). E.B. acknowledges the María Zambrano program of the Spanish Ministerio de Universidades funded by the Next Generation European Union and is also partly supported by grant RTI2018-096188-B-I00 funded by the Spanish Ministry of Science and Innovation/State Agency of Research MCIN/AEI/10.13039/501100011033. D.D., E.K.S.H., M.T.L., C.P. and L.Z. acknowledge grant support from the Space Telescope Science Institute (ID: JWST-GO-01670.007-A). OG-M acknowledges support from PAPIIT UNAM IN109123 and to the Ciencia de Frontera project CF-2023-G-100 from CONHACYT. AA, DEA and CRA acknowledge funding from the State Research Agency (AEI-MCINN) of the Spanish Ministry of Science and Innovation under the grant "Tracking active galactic nuclei feedback from parsec to kiloparsec scales", with reference PID2022-141105NB-I00. CR acknowledges support from Fondecyt Regular grant 1230345 and ANID BASAL project FB210003. MS acknowledges support by the Ministry of Science, Technological Development and Innovation of the Republic of Serbia (MSTDIRS) through contract no. 451-03-66/2024-03/200002 with the Astronomical Observatory (Belgrade). The authors acknowledge the ERS team PDRs4All (Program ID: 1228; P.I. O. N. Berné) for developing their observing program with a zero–exclusive–access period. The authors are extremely grateful to the JWST helpdesk for their constant and enthusiastic support. Finally, we thank the anonymous referee for their useful comments. This work is based on observations made with the NASA/ESA/CSA James Webb Space Telescope. The data were obtained from the Mikulski Archive for Space Telescopes at the Space Telescope Science Institute, which is operated by the Association of Universities for Research in Astronomy, Inc., under NASA contract NAS 5-03127 for JWST; and from the European JWST archive (eJWST) operated by the ESAC Science Data Centre (ESDC) of the European Space Agency. These observations are associated with programs #1049, #1050, #1228 and #1670. This paper makes use of the following ALMA data: ADS/JAO.ALMA#2017.1.00082.S, ADS/JAO.ALMA#2018.1.00113.S, ADS/JAO.ALMA#2019.1.00618.S. ALMA is a partnership of ESO (representing its member states), NSF (USA) and NINS (Japan), together with NRC (Canada) and NSC and ASIAA (Taiwan) and KASI (Republic of Korea), in cooperation with the Republic of Chile. The Joint ALMA Observatory is operated by ESO, AUI/NRAO and NAOJ. The National Radio Astronomy Observatory is a facility of the National Science Foundation operated under cooperative agreement by Associated Universities, Inc.

References

Allamandola, L. J., Tielens, A. G. G. M., & Barker, J. R. 1989, ApJS, 71, 733
Allen, M. G., Groves, B. A., Dopita, M. A., Sutherland, R. S., & Kewley, L. J. 2008, ApJS, 178, 20
Alonso-Herrero, A., Ramos, Almeida C., Esquej, P., et al. 2014, MNRAS, 443, 2766
Alonso-Herrero, A., Esquej, P., Roche, P. F., et al. 2016, MNRAS, 455, 563
Alonso-Herrero, A., Pereira-Santaella, M., García-Burillo, S., et al. 2018, ApJ, 859, 144
Alonso-Herrero, A., García-Burillo, S., Hönig, S. F., et al. 2021, A&A, 652, A99
Alonso-Herrero, A., García-Burillo, S., Pereira-Santaella, M., et al. 2023, A&A, 675, A88
Antonucci, R. 1993, ARA&A, 31, 473
Argyriou, I., Glasse, A., Law, D. R., et al. 2023, A&A, 675, A111
Arribas, S., & Mediavilla, E. 1993, ApJ, 410, 552
Audibert, A., Ramos, Almeida C., García-Burillo, S., et al. 2023, A&A, 671, L12
Baumgartner, W. H., Tueller, J., Markwardt, C. B., et al. 2013, ApJS, 207, 19
Beirão, P., Armus, L., Lehnert, M. D., et al. 2015, MNRAS, 451, 2640
Bellocchi, E., Villar Martín, M., Cabrera-Lavers, A., & Emonts, B. 2019, A&A, 626, A89
Bongiorno, A., Schulze, A., Merloni, A., et al. 2016, A&A, 588, A78
Bosman, S. E. I., Álvarez-Márquez, J., Colina, L., et al. 2024, Nat. Astron., 8, 1054
Burtscher, L., Davies, R. I., Shimizu, T. T., et al. 2021, A&A, 654, A132
Chown, R., Sidhu, A., Peeters, E., et al. 2024, A&A, 685, A75
Combes, F., García-Burillo, S., Casasola, V., et al. 2013, A&A, 558, A124
Croton, D. J., Springel, V., White, S. D. M., et al. 2006, MNRAS, 365, 11
Davies, R., Baron, D., Shimizu, T., et al. 2020, MNRAS, 498, 4150
Davies, R., Shimizu, T., Pereira-Santaella, M., et al. 2024, A&A, 689, A263
Diamond-Stanic, A. M., & Rieke, G. H. 2010, ApJ, 724, 140
Diamond-Stanic, A. M., & Rieke, G. H. 2012, ApJ, 746, 168
Donnan, F. R., García-Bernete, I., Rigopoulou, D., et al. 2023, MNRAS, 519, 3691
Donnan, F. R., García-Bernete, I., Rigopoulou, D., et al. 2024a, MNRAS, 529, 1386
Donnan, F. R., Rigopoulou, D., & García-Bernete, I. 2024b, MNRAS, 532, L75
Draine, B. T., & Li, A. 2001, ApJ, 551, 807
Draine, B. T., & Li, A. 2007, ApJ, 657, 810
Draine, B. T., Li, A., Hensley, B. S., et al. 2021, ApJ, 917, 3
Durré, M., & Mould, J. 2018, ApJ, 867, 149
Elyajouri, M., Ysard, N., Abergel, A., et al. 2024, A&A, 685, A76
Esparza-Arredondo, D., González-Martín, O., Dultzin, D., et al. 2018, ApJ, 859, 124
Esposito, F., Alonso-Herrero, A., García-Burillo, S., et al. 2024, A&A, 686, A46
Esquej, P., Alonso-Herrero, A., González-Martín, O., et al. 2014, ApJ, 780, 86
Fischer, T. C., Crenshaw, D. M., Kraemer, S. B., & Schmitt, H. R. 2013, ApJS, 209, 1

García-Bernete, I., Ramos Almeida, C., Acosta-Pulido, J. A., et al. 2015, MNRAS, 449, 1309
García-Bernete, I., Ramos Almeida, C., Landt, H., et al. 2017, MNRAS, 469, 110
García-Bernete, I., Ramos Almeida, C., Alonso-Herrero, A., et al. 2019, MNRAS, 486, 4917
García-Bernete, I., Alonso-Herrero, A., García-Burillo, S., et al. 2021, A&A, 645, A21
García-Bernete, I., González-Martín, O., Ramos Almeida, C., et al. 2022a, A&A, 667, A140
García-Bernete, I., Rigopoulou, D., Aalto, S., et al. 2022b, A&A, 663, A46
García-Bernete, I., Rigopoulou, D., Alonso-Herrero, A., et al. 2022c, MNRAS, 509, 4256
García-Bernete, I., Rigopoulou, D., Alonso-Herrero, A., et al. 2022d, A&A, 666, L5
García-Bernete, I., Alonso-Herrero, A., Rigopoulou, D., et al. 2024a, A&A, 681, L7
García-Bernete, I., Pereira-Santaella, M., González-Alfonso, E., et al. 2024b, A&A, 682, L5
García-Burillo, S., Combes, F., Usero, A., et al. 2014, A&A, 567, A125
García-Burillo, S., Combes, F., Ramos Almeida, C., et al. 2016, ApJ, 823, L12
García-Burillo, S., Combes, F., Ramos Almeida, C., et al. 2019, A&A, 632, A61
García-Burillo, S., Alonso-Herrero, A., Ramos Almeida, C., et al. 2021, A&A, 652, A98
García-Burillo, S., Hicks, E. K. S., Alonso-Herrero, A., et al. 2024, A&A, 689, A347
Gardner, J. P., Mather, J. C., Abbott, R., et al. 2023, PASP, 135, 068001
González-Martín, O., Rodríguez-Espinosa, J. M., Díaz-Santos, T., et al. 2013, A&A, 553, A35
Groves, B., Dopita, M., & Sutherland, R. 2006, A&A, 458, 405
Habart, E., Peeters, E., Berné, O., et al. 2024, A&A, 685, A73
Hermosa Muñoz, L., Alonso-Herrero, A., Pereira-Santaella, M., et al. 2024a, A&A, 690, A350
Hermosa Muñoz, L., Cazzoli, S., Márquez, I., et al. 2024b, A&A, 683, A43
Hernán-Caballero, A., & Hatziminaoglou, E. 2011, MNRAS, 414, 500
Hönig, S. F., Kishimoto, M., Gandhi, P., et al. 2010, A&A, 515, A23
Imanishi, M., Nakanishi, K., Izumi, T., & Wada, K. 2018, ApJ, 853, L25
Imanishi, M., Nguyen, D. D., Wada, K., et al. 2020, ApJ, 902, 99
Jarvis, M. E., Harrison, C. M., Mainieri, V., et al. 2021, MNRAS, 503, 1780
Jensen, J. J., Hönig, S. F., Rakshit, S., et al. 2017, MNRAS, 470, 3071
Kaneda, H., Onaka, T., Sakon, I., et al. 2008, ApJ, 684, 270
Kaufman, M. J., Wolfire, M. G., & Hollenbach, D. J. 2006, ApJ, 644, 283
Kerkeni, B., García-Bernete, I., Rigopoulou, D., et al. 2022, MNRAS, 513, 3663
Kinney, A. L., Schmitt, H. R., Clarke, C. J., et al. 2000, ApJ, 537, 152
Kristensen, L. E., Godard, B., Guillard, P., Gusdorf, A., & Pineau des Forêts, G. 2023, A&A, 675, A86
Labiano, A., García-Burillo, S., Combes, F., et al. 2013, A&A, 549, A58
Labiano, A., García-Burillo, S., Combes, F., et al. 2014, A&A, 564, A128
Labiano, A., Azzollini, R., Bailey, J., et al. 2016, SPIE, 9910, 99102W
Labiano, A., Argyriou, I., Álvarez-Márquez, J., et al. 2021, A&A, 656, A57
Lai, T. S.-Y., Armus, L. U. V., Díaz-Santos, T., et al. 2022, ApJ, 941, L36
Lai, T. S.-Y., Armus, L., Bianchin, M., et al. 2023, ApJ, 957, L26
Leach, S. 1986, J. Electron Spectros. Relat. Phenomena, 41, 427
Leach, S., Eland, J. H. D., & Price, S. D. 1989, J. Phys. Chem., 93, 7575
Li, A. 2020, NatAs, 4, 339
Li, A., & Draine, B. T. 2002, ApJ, 572, 232
Li, Y., Li, M., Yang, T., et al. 2022, Chem. Phys., 553, 111358
Martínez-Paredes, M., Alonso-Herrero, A., Aretxaga, I., et al. 2015, MNRAS, 454, 3577
Martínez-Paredes, M., Aretxaga, I., González-Martín, O., et al. 2019, ApJ, 871, 190
Mateos, S., Carrera, F. J., Barcons, X., et al. 2017, ApJ, 841, L18
McMullin, J. P., Waters, B., Schiebel, D., et al. 2007, ASP Conf. Ser., 376, 127
Morganti, R., Oosterloo, T., Oonk, J. B. R., Frieswijk, W., & Tadhunter, C. 2015, A&A, 580, A1
Nagar, N. M., Oliva, E., Marconi, A., & Maiolino, R. 2002, A&A, 391, L21
Nesvadba, N. P. H., Boulanger, F., Salomé, P., et al. 2010, A&A, 521, A65
Ogle, P., Boulanger, F., Guillard, P., et al. 2010, ApJ, 724, 1193
Ogle, P. M., López, I. E., Reynaldi, V., et al. 2024, ApJ, 962, 196
Pasquini, S., Peeters, E., Schefter, B., et al. 2024, A&A, 685, A77
Peeters, E., Spoon, H. W. W., & Tielens, A. G. G. M. 2004, ApJ, 613, 986
Peeters, E., Habart, E., Berne, O., et al. 2024, A&A, 685, A74
Peralta de Arriba, L., Alonso-Herrero, A., García-Burillo, S., et al. 2023, A&A, 675, A58
Pereira-Santaella, M., Diamond-Stanic, A. M., Alonso-Herrero, A., & Rieke, G. H. 2010, ApJ, 725, 2270
Pereira-Santaella, M., Rigopoulou, D., Farrah, D., Lebouteiller, V., & Li, J. 2017, MNRAS, 470, 1218
Pereira-Santaella, M., Álvarez-Márquez, J., García-Bernete, I., et al. 2022, A&A, 665, L11
Pier, E. A., & Krolik, J. H. 1992, ApJ, 401, 99
Ramos Almeida, C., & Ricci, C. 2017, NatAs, 1, 679
Ramos Almeida, C., Alonso-Herrero, A., Esquej, P., et al. 2014, MNRAS, 445, 1130
Ramos Almeida, C., Bischetti, M., García-Burillo, S., et al. 2022, A&A, 658, A155
Ramos Almeida, C., Esparza-Arredondo, D., González-Martín, O., et al. 2023, A&A, 669, L5
Ricci, C., Ueda, Y., Koss, M. J., et al. 2015, ApJ, 815, L13
Ricci, C., Trakhtenbrot, B., Koss, M. J., et al. 2017, ApJS, 233, 17
Rieke, G. H., Wright, G. S., Böker, T., et al. 2015, PASP, 127, 584
Rigopoulou, D., Spoon, H. W. W., Genzel, R., et al. 1999, AJ, 118, 2625
Rigopoulou, D., Barale, M., Clary, D. C., et al. 2021, MNRAS, 504, 5287
Rigopoulou, D., Donnan, F. R., García-Bernete, I., et al. 2024, MNRAS, submitted [arXiv:2406.11415]
Roche, P. F., Aitken, D. K., Smith, C. H., & Ward, M. J. 1991, MNRAS, 248, 606
Ruschel-Dutra, D., Pastoriza, M., Riffel, R., Sales, D. A., & Winge, C. 2014, MNRAS, 438, 3434
Sales, D. A., Pastoriza, M. G., Riffel, R., & Winge, C. 2013, MNRAS, 429, 2634
Schmitt, H. R., Ulvestad, J. S., Antonucci, R. R. J., & Kinney, A. L. 2001, ApJS, 132, 199
Schommer, R. A., Caldwell, N., Wilson, A. S., et al. 1988, ApJ, 324, 154
Shimizu, T. T., Davies, R. I., Lutz, D., et al. 2019, MNRAS, 490, 5860
Siebenmorgen, R., Krugel, E., & Spoon, H. W. W. 2004, A&A, 414, 123
Smajić, S., Fischer, S., Zuther, J., & Eckart, A. 2012, A&A, 544, A105
Smith, J. D. T., Draine, B. T., Dale, D. A., et al. 2007, ApJ, 656, 770
Speranza, G., Ramos Almeida, C., Acosta-Pulido, J. A., et al. 2024, A&A, 681, A63
Spilker, J. S., Phadke, K. A., Aravena, M., et al. 2023, Nature, 618, 708
Spinoglio, L., Andreani, P., & Malkan, M. A. 2002, ApJ, 572, 105
Thean, A., Pedlar, A., Kukula, M. J., Baum, S. A., & O'Dea, C. P. 2000, MNRAS, 314, 573
Thomas, A. D., Dopita, M. A., Shastri, P., et al. 2017, ApJS, 232, 11
Thornley, M. D., Schreiber, N. M. F., Lutz, D., et al. 2000, ApJ, 539, 641
Tielens, A. G. G. M. 2005, The Physics and Chemistry of the Interstellar Medium (Cambridge University Press)
Tielens, A. G. G. M. 2008, ARA&A, 46, 289
Tielens, A. 2021, Molecular Astrophysics (Cambridge: Cambridge University Press)
Venturi, G., Cresci, G., Marconi, A., et al. 2021, A&A, 648, A17
Véron-Cetty, M.-P., & Véron, P. 2006, A&A, 455, 773
Voit, G. M. 1992, MNRAS, 258, 841
Wenzel, G., Joblin, C., Giuliani, A., et al. 2020, A&A, 641, A98
Wilson, A. S., Baldwin, J. A., & Ulvestad, J. S. 1985, ApJ, 291, 627
Wilson, A. S., Braatz, J. A., Heckman, T. M., Krolik, J. H., & Miley, G. K. 1993, ApJ, 419, L61
Wright, G. S., Wright, D., Goodson, G. B., et al. 2015, PASP, 127, 595
Zhang, L., & Ho, L. C. 2023a, ApJ, 943, 60
Zhang, L., & Ho, L. C. 2023b, ApJ, 953, L9
Zhang, L., Ho, L. C., & Li, A. 2022, ApJ, 939, 22
Zhang, L., Packham, C., Hicks, E. K. S., et al. 2024a, ApJ, submitted [arXiv:2409.09771]
Zhang, L., García-Bernete, I., Packham, C., et al. 2024b, ApJ, submitted [arXiv:2409.09772]

[1] Centro de Astrobiología (CAB), CSIC-INTA, Camino Bajo del Castillo s/n, E-28692 Villanueva de la Cañada, Madrid, Spain
[2] Department of Physics, University of Oxford, Keble Road, Oxford OX1 3RH, UK
[3] School of Sciences, European University Cyprus, Diogenes street, Engomi, 1516 Nicosia, Cyprus
[4] Instituto de Física Fundamental, CSIC, Calle Serrano 123, 28006 Madrid, Spain
[5] Max-Planck-Institut fur extraterrestrische Physik, Postfach 1312, D-85741 Garching, Germany
[6] Observatorio Astronómico Nacional (OAN-IGN)-Observatorio de Madrid, Alfonso XII, 3, 28014 Madrid, Spain

[7] Telespazio UK for the European Space Agency (ESA), ESAC, Camino Bajo del Castillo s/n, 28692 Villanueva de la Cañada, Spain
[8] Department of Physics and Astronomy, The University of Texas at San Antonio, 1 UTSA Circle, San Antonio, Texas 78249-0600, USA
[9] Instituto de Astrofísica de Canarias, Calle Vía Láctea, s/n, E-38205 La Laguna, Tenerife, Spain
[10] Departamento de Astrofísica, Universidad de La Laguna, E-38206 La Laguna, Tenerife, Spain
[11] Departmento de Física de la Tierra y Astrofísica, Fac. de CC Físicas, Universidad Complutense de Madrid, 28040 Madrid, Spain
[12] Instituto de Física de Partículas y del Cosmos IPARCOS, Fac. CC Físicas, Universidad Complutense de Madrid, 28040 Madrid, Spain
[13] LERMA, Observatoire de Paris, Collège de France, PSL University, CNRS, Sorbonne University, Paris, France
[14] Department of Physics and Astronomy, University of Alaska Anchorage, Anchorage, AK 99508-4664, USA
[15] School of Physics & Astronomy, University of Southampton, Highfield, Southampton SO171BJ, UK
[16] Instituto de Radioastronomía and Astrofísica (IRyA-UNAM), 3-72 (Xangari), 8701 Morelia, Mexico
[17] National Astronomical Observatory of Japan, National Institutes of Natural Sciences (NINS), 2-21-1 Osawa, Mitaka, Tokyo 181-8588, Japan
[18] Department of Astronomy, School of Science, The Graduate University for Advanced Studies, SOKENDAI, Mitaka, Tokyo 181-8588, Japan
[19] Space Telescope Science Institute, 3700 San Martin Drive, Baltimore, Maryland 21218, USA
[20] Kavli Institute for Particle Astrophysics & Cosmology (KIPAC), Stanford University, Stanford, CA 94305, USA
[21] Instituto de Estudios Astrofísicos, Facultad de Ingeniería y Ciencias, Universidad Diego Portales, Avenida Ejercito Libertador 441, Santiago, Chile
[22] Astronomical Observatory, Volgina 7, 11060 Belgrade, Serbia
[23] Sterrenkundig Observatorium, Universiteit Gent, Krijgslaan 281-S9, Gent B-9000, Belgium
[24] Centro de Astrobiología (CAB), CSIC-INTA, Ctra. de Ajalvir, km 4, 28850 Torrejón de Ardoz, Madrid, Spain
[25] Centre for Extragalactic Astronomy, Durham University, South Road, Durham DH1 3LE, UK

Appendix A: Mid-IR modelling and aperture selection

We extracted the JWST/MRS spectra from the nuclear regions of the three sources studied here following the same method as in García-Bernete et al. (2024a). In addition, we selected a number of circumnuclear regions in the three targets to investigate similarities and differences in the PAH properties between nuclear regions and outflow and star-forming zones. For the extended emission, we use apertures ranging of 1.″0 and 1.″5 diameter (see Fig. A.1).

To fit the mid-IR continuum and in particular the PAH emission features of star-forming regions we use a modified version of PAHFIT (Smith et al. 2007) to work with the higher spectral resolution JWST data (Donnan et al. 2023). However, PAHFIT does not produce successful fits for the nuclear regions of the sources studied here due to the complexity of the dust continuum and the high levels of extinction present. Therefore, we use a novel technique using a differential extinction model (i.e. the strength of extinction varies with wavelength) which probes different layers of the dust and produces satisfactory fits to deeply obscured sources (Donnan et al. 2024a). We note that the newly developed model is in agreement with PAHFIT for relatively unobscured sources as star-forming regions. We refer the reader to Donnan et al. (2024a) for a full description of the model. The fits for the nuclear regions of NGC 5506 and NGC 5728 are shown in Fig. A.2. In Fig. A.3 we show an example of a fit for a SF-dominated region. In Tables A.1, A.2, and A.3, we list the fluxes of the MIR PAH features for the nuclear, circumnuclear regions, and Orion Bar, respectively.

We selected a number of circumnuclear regions in NGC 5506, NGC 5728 and NGC 7172. Considering the morphology of the circumnuclear emission of the sources (see Sect. 4), we chose regions including emission along the SF ring (1″diameter extraction apertures), the outflow (1.5″diameter extraction apertures) and high-velocity dispersion region (perpendicular to the jet; 1.5″diameter extraction apertures) and galaxy disks of NGC 5506 and NGC 7172 (1.5″diameter extraction apertures). Given the geometry of NGC 5506 and NGC 7172 (e.g. Esposito et al. 2024; Hermosa Muñoz et al. 2024a), the outflow is located behind the disk for the southern region of NGC 5506 (Disk3) and the northern region of NGC 7172 (Disk3). Therefore, these regions show values of their PAH ratios similar to those of the disk. In Fig. A.4 we present the same PAH diagram as in Fig. 5 but including all the individual regions.

Appendix B: Orion Bar

For comparison, we also include in our analysis observations of the Orion Bar, which have been already presented in Chown et al. (2024), Habart et al. (2024), Peeters et al. (2024), Pasquini et al. (2024) and Elyajouri et al. (2024)). This was observed was taken using JWST as part of the Director's Discretionary Early Release Science (ERS) Program ID: 1228 (P.I. O. N. Berné). The extracted spectra consist of a H II , an atomic PDR and three regions of dissociation fronts (DF1, DF2, DF3) (see e.g. Fig. 1 of Peeters et al. 2024). In particular, we use the fully reduced version of the spectra presented in Chown et al. (2024), which are publicly available in webpage[9] of the ERS team PDRs4All. Using these spectra, we measured the PAH ratios (see Table A.3 using the same method as in Appendix A.

[9] https://pdrs4all.org/seps/

Appendix C: Notes on individual objects

C.1. NGC 5728

NGC 5728 is a type 2 AGN also classified as Compton-thick AGN (Véron-Cetty & Véron 2006). It has a circumnuclear stellar ring (~800 pc; e.g. Schommer et al. 1988; Durré & Mould 2018; Shimizu et al. 2019 and references therein) and large stellar bar (~11 Kpc; Schommer et al. 1988; Durré & Mould 2018). NGC 5728 also presents ionisation cones detected in [O III] and Hα (~1.5 kpc; PA~120) at both sizes of the nucleus (e.g. Schommer et al. 1988; Arribas & Mediavilla 1993; Wilson et al. 1993; Durré & Mould 2018; Shimizu et al. 2019). In the same orientation, 6 and 20 cm radio observations show a compact radio core with one-sided which is related to the emission of a radio jet (Schommer et al. 1988; Durré & Mould 2018). Figure C.1 shows a sketch summarising the geometry model derived by Shimizu et al. (2019). Note that the position angle of the cone has been updated to that used in Davies et al. (2024) (i.e. position angle of -60° with an opening angle of ±30°. The 3D scheme show the strong geometrical coupling between the AGN outflow (and jet) and the host galaxy disk.

NGC 5728 has a star-foming ring of ~1 kpc size, showing several bright [Ne II] clumps (see Davies et al. 2024). The high IP (e.g. [Ne V] and [S V]) emission line maps show the prominent ionisation cones in the galaxy (see Fig. 2). This region coincides with outflow located in the SE to NW direction (see Fig. 2; also Durré & Mould 2018; Shimizu et al. 2019). We also note that MIRI/MRS velocity dispersion maps of [Ne III], [Ne V] and [S V] reveal a high-velocity dispersion region in an almost perpendicular region of the main axis of the outflow (see Fig. 4; also Davies et al. 2024). Durré & Mould (2018) has also proposed the presence of a nuclear bar in the optical ratios. The [Fe II] intensity map shows the presence of shocks operating in the ionisation cones orientation (see Fig. 2).

C.2. NGC 5506

NGC 5506 is classified as a narrow-line Sy 1 or type 2 AGN (see Nagar et al. 2002 for further discussion). Moreover, the host galaxy disk is close to edge-on (i_{disk} ~ 76°; Fischer et al. 2013) and, thus, dust in the galaxy disk might be responsible for a significant part of the nuclear obscuration. The NLR bicone emission is extended over a few kpc and elongated in the north-south direction (Wilson et al. 1985; Fischer et al. 2013). Also, VLA radio observations show a compact nucleus and a radio jet is extended along PA~70° and i~82° (Kinney et al. 2000). In Fischer et al. (2013, their Fig. 21), the authors showed the geometry of NGC 5506 derived from the NLR modeling (similarly as in Fig. C.1).

C.3. NGC 7172

NGC 7172 hosts a type 2 AGN with a prominent dust lane (e.g. Smajić et al. 2012 and references therein). A two-sided ionisation cones with broad opening angle (~120°) is detected by using optical integral field spectroscopy (e.g. Thomas et al. 2017). ALMA CO(3-2) observations showed the presence of a cold molecular gas ring (~500-700 pc), which is not only rotating but also outflowing (e.g. Alonso-Herrero et al. 2023). VLA observations detected a nuclear point-like emission and faint radio emission elongated to the northeast and southwest of the nucleus (e.g. Thean et al. 2000). This faint radio emission located in the same orientation as the ionised cone, which suggest that might

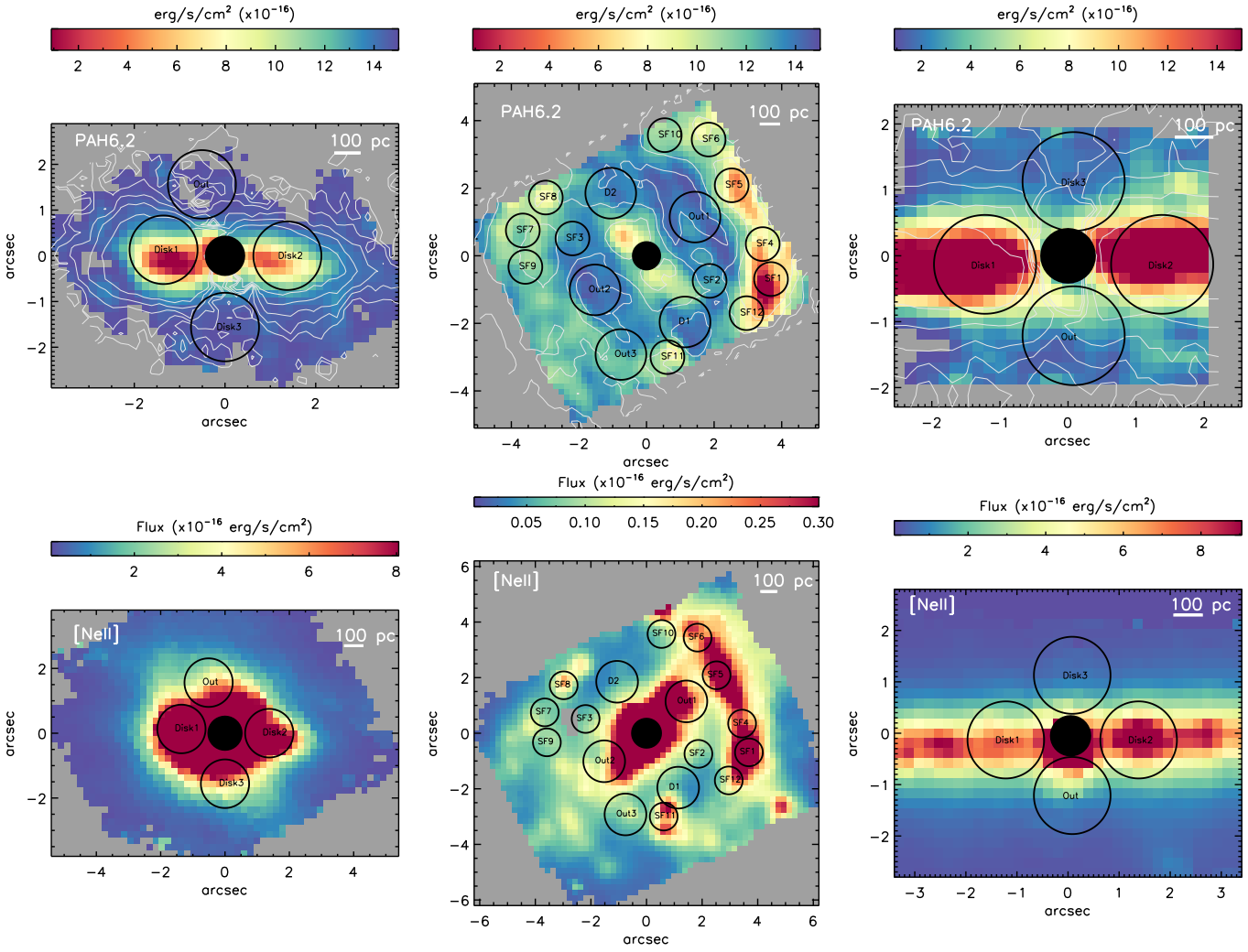

Fig. A.1. Maps showing the selected apertures. From left to right panels: NGC 5506, NCG 5728 and NGC 7172. Top panels: 6.2 μm PAH feature intensity map. The white contours are the 11.3 μm PAH emission on a logarithmic scale (same values as in bottom panels of Fig. 3). Bottom panels: [Ne II] 12.81 μm intensity map. North is up and east is to the left, and offsets are measured relative to the AGN. Black circles correspond with the extracted apertures.

Table A.1. Nuclear PAH measurements. Fluxes and errors are in units of 10^{-14} erg s^{-1} cm^{-2}.

Galaxy (1)	PAHλ6.2μm (2)	PAHλ7.7μm (3)	PAHλ8.6μm (4)	PAHλ11.3μm (5)	PAHλ17.0μm (6)
NGC 5506	<13.5	88.30	0.13	49.53	<84.70
NGC 5728	<3.47	26.82	1.22	12.32	<19.63
NGC 7172	...	...	....	....	....

be related with a low power radio jet (e.g. Alonso-Herrero et al. 2023).

Table A.2. Circumnuclear PAH measurements. Fluxes are in units of 10^{-14} erg s^{-1} cm^{-2}.

Region (1)	PAHλ6.2μm (2)	PAHλ7.7μm (3)	PAHλ8.6μm (4)	PAHλ11.3μm (5)	PAHλ12.7μm (6)	PAHλ17.0μm (7)
NGC 5728-SF1	5.65	17.66	3.90	5.33	3.59	2.12
NGC 5728-SF2	1.61	2.72	0.54	2.09	1.35	0.97
NGC 5728-SF3	1.28	4.48	0.97	3.85	2.44	1.70
NGC 5728-SF4	4.16	11.18	2.12	4.32	2.80	2.10
NGC 5728-SF5	4.56	14.67	2.93	5.94	3.81	2.39
NGC 5728-SF6	2.46	7.36	1.36	3.85	2.52	1.43
NGC 5728-SF7	1.91	6.41	1.46	3.36	1.87	1.49
NGC 5728-SF8	2.41	8.79	1.70	2.80	2.61	1.93
NGC 5728-SF9	1.99	5.97	1.38	4.02	2.25	1.83
NGC 5728-SF10	1.94	5.49	1.18	2.86	1.99	1.02
NGC 5728-SF11	2.50	8.63	1.97	2.73	2.06	1.30
NGC 5728-SF12	3.71	13.13	2.83	4.61	3.51	1.91
NGC 5728-D1	2.68	6.82	1.84	3.38	2.31	3.62
NGC 5728-D2	2.24	7.26	1.46	4.34	2.62	2.42
NGC 5728-Out1	1.82	5.16	1.10	3.57	2.19	1.76
NGC 5728-Out2	2.08	7.56	1.53	4.54	2.78	3.38
NGC 5728-Out3	3.80	9.83	2.09	5.41	3.14	2.25
NGC 5506-Disk1	54.85	214.01	54.65	53.37	31.77	20.35
NGC 5506-Disk2	45.80	194.97	41.07	57.03	45.37	19.79
NGC 5506-Disk3	4.11	19.53	5.33	5.45	15.13	8.84
NGC 5506-Out	4.82	27.47	7.11	13.38	17.99	4.06
NGC 7172-Disk1	42.56	204.19	23.89	57.62	39.74	11.40
NGC 7172-Disk2	34.76	172.98	22.45	50.80	40.38	17.48
NGC 7172-Disk3	13.62	58.86	8.33	20.16	9.43	3.01
NGC 7172-Out	7.79	46.91	5.15	29.53	12.39	1.39

Table A.3. PAH ratios of Orion from the measurements described in Appendix B.

Region (1)	6.2/7.7 μm PAH ratio (2)	11.3/7.7 μm PAH ratio (3)	Ref. (4)
Orion H II region (d=0.224 pc to θ^1 Ori C)	0.35±0.05	0.63±0.05	This work
Orion atomic PDR	0.34±0.05	0.31±0.03	This work
Orion dissociation front 1	0.38±0.07	0.29±0.03	This work
Orion dissociation front 2	0.37±0.06	0.35±0.04	This work
Orion dissociation front 3	0.33±0.04	0.33±0.03	This work
NGC 6552 (AGN)	0.22±0.03	0.43±0.05	García-Bernete et al. 2022d
NGC 7319 (AGN)	[0.22-0.31]	<1.75	García-Bernete et al. 2022d
NGC 7469 (AGN)	0.31±0.04	0.53±0.05	García-Bernete et al. 2022d
Average SF regions of NGC 3256	0.30±0.02	0.29±0.02	Rigopoulou et al. 2024
Average SF-ring of NGC 7469	0.29±0.06	0.23±0.05	García-Bernete et al. 2022d

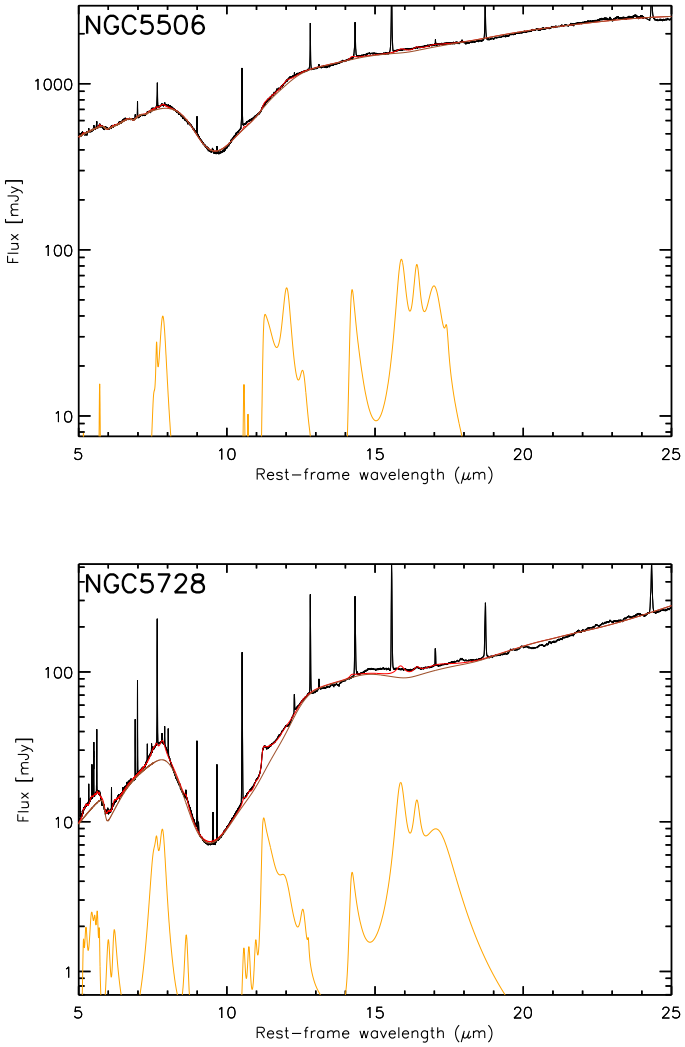

Fig. A.2. Mid-IR spectral modelling of the nuclear regions of NGC 5506 (top panel) and NGC 5728 (bottom panel). The JWST/MRS rest-frame spectra and model fits correspond to the black and red solid lines. We show the continuum (brown solid lines) and the fitted PAH features (orange solid lines). Note that NGC 7172 does not show nuclear PAH emission and, thus, it is not included in this plot.

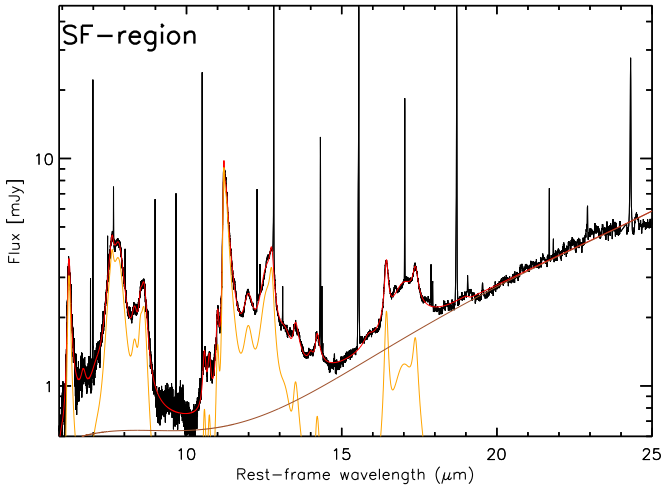

Fig. A.3. Example of the mid-IR spectral modelling of a SF-dominated region of NGC 5728. The JWST/MRS rest-frame spectra and model fits correspond to the black and red solid lines. We show the continuum (brown solid lines) and the fitted PAH features (orange solid lines).

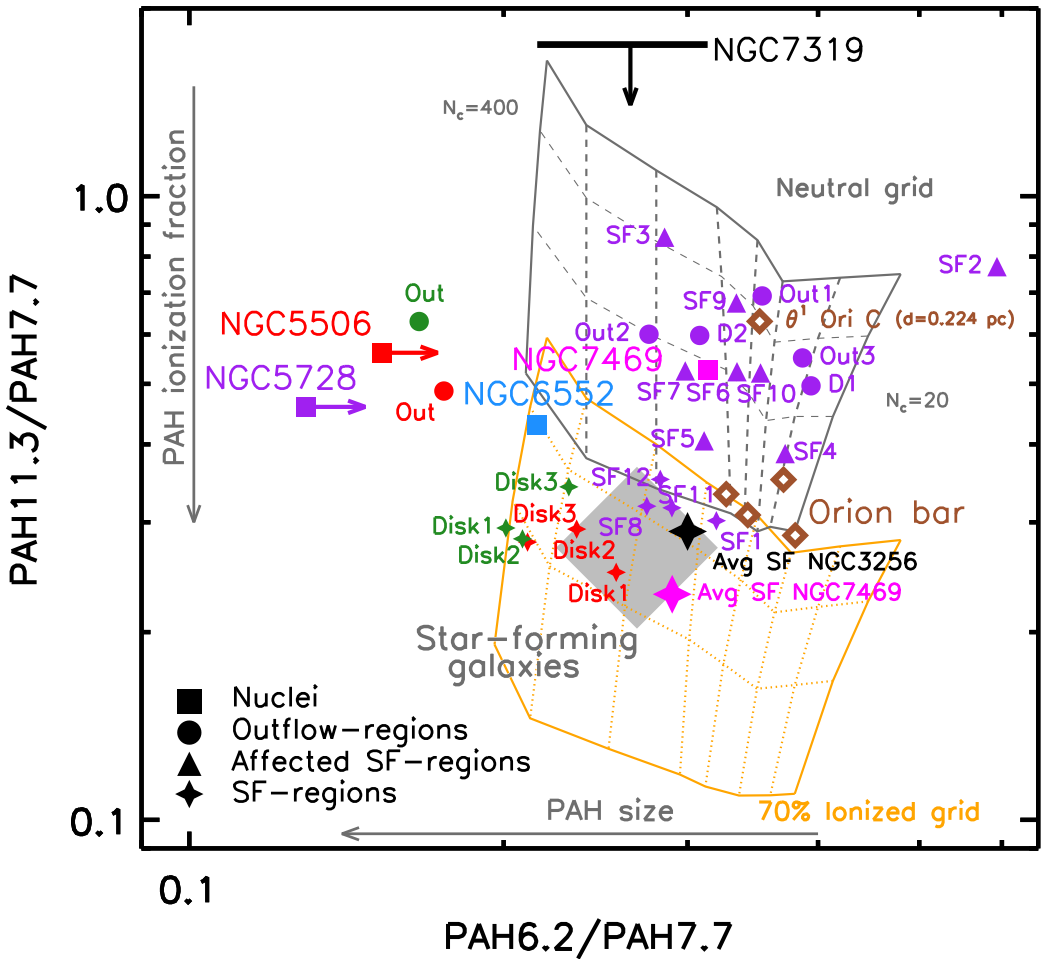

Fig. A.4. Same as Fig. 5, but including all the individual regions. In Tables A.1, A.2, and A.3 we list the measured PAH fluxes.

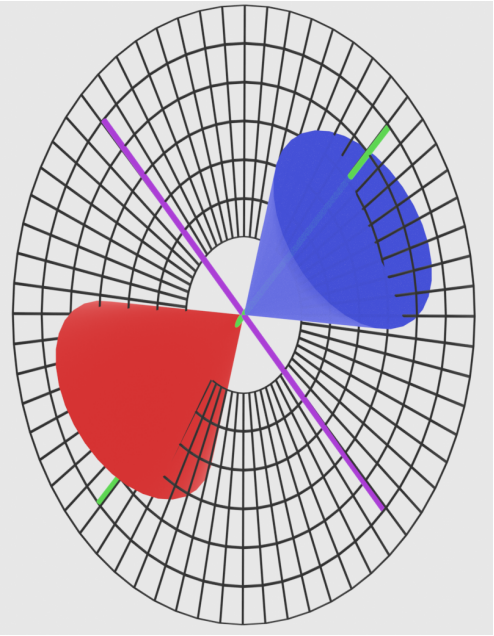

Fig. C.1. 3D scheme for the geometry of NGC 5728 derived from the NLR modeling by Shimizu et al. (2019). Note that the position angle of the cone has been updated to that used in Davies et al. (2024). The bicone indicates the AGN outflow (blue and redshifted velocities). The green line represents the jet axis. The purple line correspond to the perpendicular direction of the jet-axis (i.e. high velocity dispersion region in Fig. 4). North is up and east is left.